Measuring the size of non-spherical particles and the implications for grain size analysis in volcanology

Hannah M. Buckland[1*]**,** Jennifer Saxby[2], Matt Roche[1], Phoebe Meredith[1], Alison C. Rust[1], Katharine V. Cashman[1] and Samantha L. Engwell[3]

1. School of Earth Sciences, University of Bristol, Wills Memorial Building, Bristol, UK
2. School of Earth and Environment, University of Leeds, Leeds, UK
3. British Geological Survey, The Lyell Centre, Edinburgh, UK

*Corresponding author email address: hannah.buckland@bristol.ac.uk

ABSTRACT

1. Introduction

Particles with highly irregular shapes, such as the products of explosive volcanic eruptions (tephra), present a particular challenge when quantifying particle size. The ‘size’ of non-spherical particles can be quantified in multiple ways depending on the method of measurement and definition of ‘size’. For example, size can be measured as the longest particle dimension using callipers, or the diameter of a volume equivalent sphere calculated from 3D data (Bagheri et al. 2015; Saxby et al. 2020). A clear and consistent definition of size is important because the ‘size’ of tephra is used to predict the dispersal of the particles in the atmosphere (Rose and Durant 2009; Mele et al. 2011; Engwell and Eychenne 2016; Saxby et al. 2018). The grain size distribution (GSD) of tephra also provides insight into fragmentation mechanisms (e.g. Barberi et al. 1989; Wohletz et al. 1989; Jones et al. 2016; Mele et al. 2020) and estimates of eruption column heights for unobserved eruptions (e.g. Carey and Sparks 1986; Burden et al. 2011; Rossi et al. 2019). The GSD of volcanic ash (tephra <2 mm) is also important for understanding the risks posed to human health and infrastructure (Horwell and Baxter 2006; Horwell 2007; Bebbington et al. 2008; Wilson et al. 2012; Blake et al. 2017) and the efficiency of wind-driven remobilisation (Hadley et al. 2004; Leadbetter et al. 2012; Liu et al. 2014; Panebianco et al. 2017). Finally, quantitative measurements of particle shape complement size analysis and are equally important for interpreting eruptive processes and forecasting tephra transport and sedimentation (Heiken 1972; Riley et al. 2003; Cioni et al. 2014; Liu et al. 2015; Bagheri et al. 2015; Saxby et al. 2018; Dürig et al. 2020).

One of the main challenges faced when characterising a tephra deposit is the large range of particle sizes produced by an eruption (from 10^{-6} - 10^{1} m). This has required use of a variety of methods to measure size, often requiring an overlap of two or more methods to analyse the coarse and fine components of a single sample. Numerous size and shape parameters are associated with different methods and the choice of parameter has implications for data interpretation and comparison. Furthermore, particle size and shape are typically analysed separately using different methods, leading to slow data collection and processing as noted by several authors who have investigated the range of shape parameters and size characterisation methods for volcanic ash (Riley et al. 2003; Liu et al. 2015; Leibrandt and Le Pennec 2015). Thus, despite the importance of grain size and shape characterisation, data compilation and comparison across different studies is hindered by the range of methods used.

Tephra from a single eruption is a mixture of components (e.g., lithics, free-crystals and juvenile fragments such as pumice) and each component can have unique optical and physical properties (e.g., refractive index, density, porosity and permeability) which can limit the efficacy of grain size methods initially developed for analysing more homogenous materials. Furthermore, the different components within a single sample, such as free-crystals, can have individual GSDs that overlap to produce the GSD of the whole sample (Moore 1934; Walker 1971; Sparks 1976; Mele et al. 2020). A further complication is that the componentry can vary spatially in a deposit due to emplacement and transport processes (Sparks and Walker 1977; Carey and Sigurdsson 1982; Williams and Self 1983; Eychenne et al. 2015). For example, crystal concentrations observed in airfall deposits reflect a narrow crystal size and density distribution that causes deposition over a limited transport distance. Grain size procedures that do not account for variations in particle density or componentry with size (e.g., sieving) could therefore produce inaccurate interpretations of GSDs.

Here we outline an analytical protocol for simultaneous size and shape characterisation using a fast and flexible method that employs dynamic image analysis (DIA). Methods of size measurement that use image analysis do not need to assume particle shape, which is analysed simultaneously. Imaging the particles also means that multiple size parameters (e.g., particle long axis and equivalent circle diameter) are measured concurrently. This provides flexibility and consistency when reporting size measurements. First we review methods of grain size measurement (Section 2; Table 1), expanding on the summary by Eychenne and Engwell (2016) and with emphasis on how ‘size’ is quantified. We then outline the methodology for size analysis using DIA with example analyses using spherical and non-spherical particles (Section 3). We then discuss the benefits of DIA for measuring the grain size of tephra and examine the implications of different size measurements in volcanological applications (Sections 4-5). We conclude by showing ways in which inconsistencies in size definitions for non-spherical particles affect studies of explosive volcanism, particularly when particle shapes are extreme, as is common for glass shards.

2. Background

Analysing the grain size of tephra is a long-established practise in volcanology and the standard methodologies were adopted from the wider field of sedimentology (Wentworth 1922; Krumbein 1934; Pettijohn 1949). For example, early work characterising the grain size of field deposits helped distinguish poorly sorted pyroclastic density current deposits (nuée ardente or ignimbrite deposits) from well sorted airfall deposits (Lacroix 1904; Moore 1934; Fenner 1937). Standard statistical procedures from sedimentology were also adopted, such as characterising GSDs using the maximum clast size, median diameter (Md) and sorting (σ; Fisher 1964). Also adapted from sedimentology is the practise of deconvolving multi-modal GSDs into sub-populations. Studies of sands attribute sub-populations in multi-modal GSDs to the genesis of the material (Visher 1969) and when applied to volcanic GSDs, grain size sub-populations are related to eruptive processes (Sheridan 1971; Wohletz et al. 1989; Eychenne et al. 2015). Whilst these procedures have merit and can provide insight into volcanic processes, the complex and heterogeneous physical properties of tephra suggests that volcanic GSDs measured using traditional grain size methods may need additional scrutiny.

2.1. Why is grain size important for volcanology?

Grain size data are used to interpret two key eruption source parameters (ESPs), the eruption column height (Carey and Sparks 1986; Woods and Wohletz 1991; Sparks et al. 1992; Burden et al. 2011) and the total grain size distribution (TGSD; Carey and Sigurdsson 1982; Bonadonna and Houghton 2005). Both parameters are used to interpret the nature of eruptive activity from field deposits. Eruption column height can be inferred from modelled clast support envelopes within the eruption column (Carey and Sparks 1986) and requires maximum clast size data that are typically measured in the field on a subsample of the largest clasts (Bonadonna et al. 2013). TGSDs are produced by combining GSDs from multiple sampling sites across the tephra deposit and weighting them according to the mass accumulation of tephra (Carey and Sigurdsson 1982; Bonadonna and Houghton 2005). Here GSD is in reference to tephra that has been deposited on the ground.

ESPs are a key requirement for ash dispersion models, which can be used to reconstruct past eruptions or to forecast tephra dispersal from future eruptions (Mastin et al. 2009; Webley et al. 2009; Bonadonna et al. 2012; Beckett et al. 2015). Most operational and research-based ash dispersion models use an input particle size distribution (PSD), where PSD is used in reference to tephra in the atmosphere (Mastin et al. 2009; Bonadonna et al. 2012; Beckett et al. 2015; WMO 2018). TGSDs can be used to inform PSDs but there are several challenges to relating the two measures. First, TGSD estimates are sensitive to both the spatial coverage and the number of individual GSDs measured (Bonadonna and Houghton 2005; Alfano et al. 2016; Pioli et al. 2019). This sensitivity can propagate as uncertainty in the outputs of dispersion models if TGSDs are used as input PSDs (Beckett et al. 2015). Secondly, most ash dispersion model PSDs describe a distribution of spherical particles (or particles with a fixed shape factor; Beckett et al. 2015; Saxby et al. 2018). Therefore, equating measured TGSDs directly to PSDs is not appropriate where particle shapes are not constant and 'size' measurements vary with particle shape and/or other physical properties such as density or refractive index.

An alternative to using TGSDs for ash dispersion modelling is to use PSDs that have been measured in situ from an active plume. In situ PSDs have been measured following aircraft encounters with ash clouds (Hobbs et al. 1991; Casadevall 1994; Pieri et al. 2002), by flying sampling devices through plumes (e.g. Johnson et al. 2012; Petäjä et al. 2012; Mori et al. 2016; Schellenberg et al. 2019), from satellite retrievals (e.g. Prata and Grant 2001; Bonadonna et al. 2011; Pavolonis et al. 2013; Gouhier et al. 2019) and using ground based sensors (Scollo et al. 2005; Bonadonna et al. 2011; Kozono et al. 2019). However, in situ measurements are limited to a small number of modern eruptions and the range of grain sizes is never fully covered by one technique. Furthermore, how 'size' is quantified is not consistent across ground-based or in situ techniques, which makes the combination and comparison of in situ PSDs and GSDs challenging (Bonadonna et al. 2011; Stevenson et al. 2015).

2.2. Grain size methods in volcanology

2.2.1. Coarse sieving

The GSD of coarse (>125 μm) unconsolidated tephra is typically measured by sieving. The tephra is passed through a series of nested sieves where the aperture size typically decreases on the logarithmic φ or Krumbein scale (Krumbein 1934) in whole-φ, half-φ or quarter-φ increments where

$$\varphi = -log_2 d \qquad (1)$$

and *d* is the length of the side of the square aperture in mm. The φ-scale is widely used in sedimentology and volcanology instead of an arithmetic or linear scale to avoid emphasis of this mass-based measure on the coarse sediment (Blott and Pye 2001). Manual or mechanical shaking, with or without the addition of water, is used to segregate the tephra into the individual sieve fractions. The minimum particle "size" (diameter for a sphere) within a sieve fraction is equal to *d*. The GSD is then reported as the percentage of the analysed mass (weight percent) retained in each sieve fraction.

Sieving is a low cost and established method that is often the only available tool for measuring very coarse size fractions whilst in the field (Folk and Ward 1957; Walker 1971; Fairbridge and Bourgeois 1978). However, sieving does have limitations. Firstly, the sieve size is only equal to the particle size for spheres. Anisotropic particle shapes mean that clasts do not always pass through the sieve mesh according to the same dimension. For example, flat or elongated particles can be sorted according to their largest or smallest dimension which can vary substantially (e.g. needle like particles in Katla SILK layers; Saxby et al. 2018, 2020). This means that sieving sorts by both size and shape (Komar and Cui 1984). Agitation of delicate tephra when sieving can also lead to clast breakage and alteration of the GSD and particle shape during analysis (Cox et al. 2017) so the reproducibility of the GSD depends on the method and duration of agitation. The amount of material sieved affects the ease of GSD measurement, particularly for coarse material where large quantities of material are required to ensure a representative aliquot (Swineford and Swineford 1946; Sarocchi et al. 2011; Román-Sierra et al. 2013). Interpretations of GSDs produced by sieving also depend on the sieve interval. Ideally, sieve intervals should be quarter- or half-φ, because larger intervals present difficulties in computing statistics, especially for fractions >2 mm (-1 φ; Hails et al. 1973). The grain size range typically covered by sieves is from ~125 mm to 20 µm (Table 1). However, sieving below ~125 µm is challenging as fine sieves are prone to overloading, and fine material can form coarser aggregates or loft when agitated meaning that the particles do not pass into the correct sieve fraction and can be lost. For this reason, other methods are preferred for measuring particles <125 µm.

2.2.2. Particle sedimentation

An alternative method of grain size analysis uses rates of particle sedimentation; this method measures the velocities of particles settling in a fluid of known viscosity and density and can cover a wide range of particle sizes (~50 – 5000 µm; Table 1; Gibbs et al. 1971). From the measured settling velocities, the diameters of dense equivalent spheres that would have the same settling velocities are calculated using an empirical equation (Gibbs et al. 1971). A variant is the pipette method, which uses water as the fluid and has been used with volcanic tephra (Watanabe et al. 1999; Wiesner et al. 2004). Another sedimentation method is the Roller apparatus (Roller 1931; Riley et al. 2003), an air elutriation device that separates particles according to their settling velocities in air. As with sieving, however, sedimentation methods of grain size analysis indirectly measure the effects of grain shape, and specifically for these methods, variations in particle density (Sanford and Swift 1971; Komar and Cui 1984; Beuselinck et al. 1998). Moreover, the settling behaviour of fine material (<125 µm) is poorly described by existing settling laws because of aggregation, Brownian motion (<10 µm) and complex flow and depositional regimes (Rose and Durant 2009; Brown et al. 2012; Engwell and Eychenne 2016; Saxby et al. 2018).

Table 1 – Summary of grain size methods discussed in this study with measurement range and the assumptions required to quantify size.

Method name	Measurement range (µm)	Method assumptions	Size measure	Mass or volume distribution
Sieving	20 - 125000	Sieve apeture only equal to particle size if spherical	Diameter for spheres, minimum to intermediate dimension for non-spherical particles	M
Pipette method	50 - 5000	Constant density spheres	Equivalent settling velocity sphere diameter	V
Roller apparatus	1 - 100	Settling velocity classes of constant density spheres	Equivalent settling velocity sphere diameter	V
Laser diffraction (Mie theory)	0.01 - 3500	Spherical particles, constant refractive index	Volume equivalent sphere diameter	V
Laser diffraction (Fraunhofer approximation)	10 - 3500	Flat disc particles, particles only cause diffraction	Maximum width	V
Electrozone sensing (e.g. Coulter counter)	0.4 - 1600	Spherical particles	Volume equivalent sphere diameter	V
Image analysis (SEM)	~0.01 - 200	Conversion from 2D area to 3D volume	2D Miscellaneous	V
Image analysis (Morphologi)	0.5 - 1300	Conversion from 2D area to 3D volume	2D Miscellaneous	V
Image analysis (cryptotephra)	20 - 250	Conversion from 2D area to 3D volume, material <20 µm removed	2D Miscellaneous	V
Radar disdrometer (e.g. PLUDIX)	1000 - 10000	Dense spherical particles	Volume equivalent sphere diameter	V
Laser disdrometer (e.g. Parsivel2)	200 - 25000	Dense spherical particles	Volume equivalent sphere diameter or maximum width	V
High resolution video	62 - 2000	Conversion from 2D area to 3D volume	2D Miscellaneous	V
Satellite infrared retreivals	~0 - 100	Spherical particles, constant refractive index	Volume equivalent sphere diameter	V
Dynamic image analysis (e.g. Camsizer X2)	0.8 - 8000	Conversion from 2D area to 3D volume	2D Miscellaneous	V

2.2.3. Laser diffraction

Laser diffraction is the most common method used in volcanology to characterise the GSD of fine material (e.g. Horwell 2007; Buckland et al. 2018; Genareau et al. 2019). The sample is dispersed in a liquid (commonly distilled water) to form a suspension that passes by three lasers with different wavelengths. The diffraction of the laser beams by the suspended particles is used to calculate particle size by inverting the measured scattering pattern. The GSD is then output as a volume distribution; combining laser diffraction data with sieve data thus requires estimates of particle density. This method is rapid (<2 mins per analysis) and instruments such as the Mastersizer 3000 by Malvern Panalytical (formerly Malvern Instruments Ltd) can measure a particle size range of 0.01 – 3500 µm (Malvern Panalytical 2020). However, the mathematical model chosen to resolve the laser scattering can introduce errors. For example, Mie scattering theory assumes spherical particles and requires an assumption of refractive index. Tephra is very rarely close to spherical, however, and the refractive index is not routinely measured. Moreover, as tephra is commonly a mixture of crystals, lithics and glass, one refractive index will not be representative of the whole sample. An alternative mathematical model used to resolve the laser scattering is the Fraunhofer theory, which assumes particles are flat discs and that the particles only cause diffraction, thus it does not require an assumption of refractive index (Beuselinck et al. 1998; Cyr and Tagnit-Hamou 2001). However, the Fraunhofer approximation can overestimate the proportion of very fine particles (<10 µm) due to this simplification (Cyr and Tagnit-Hamou 2001).

2.2.4. Electrozone sensing

Another method of characterising the GSD of fine material is electrozone sensing, or the Coulter counter method, which has a measurement range of ~0.4 – 1600 µm. This requires that particles are suspended in an electrically conductive fluid. The suspended particles are counted as they pass through an aperture of known diameter which generates a pulse in electrical resistivity that is measured and related to an equivalent sphere diameter based on the calibration curve of the instrument (Figueiredo 2006). The resulting GSD can be output either as a number (particle count) or volume (converted from equivalent sphere diameter) distribution. This method has been used to measure the GSD of volcanic ash (e.g.

Sparks et al. 1983; Carey et al. 1988; Brand et al. 2016) and has the benefit of being non-optical and therefore not affected by variations in particle opacity or reflectivity. However, similar to particle sedimentation methods, both electrozone sensing and laser diffraction methods quantify size as an equivalent sphere diameter and provide no information about particle shape.

2.2.5. Grain size analysis from image analysis

Image analysis is a flexible method for characterising the grain size and shape of coarse- and fine-grained materials. Here we focus on the application of image analysis to determine the GSD for fine-grained materials, but there are a number of studies that use image analysis to determine the GSD of coarse and consolidated volcanic material (e.g. Capaccioni et al. 1997; Sarocchi et al. 2011; Jutzeler et al. 2012). The grain size of fine ash can be characterised using scanning electron microscope (SEM) images, most commonly collected in secondary electron mode (SE; Riley et al. 2003; Horwell et al. 2003; Coltelli et al. 2008; Liu et al. 2015). This method allows simultaneous classification of particle shape and componentry (lithic, glass or crystal). However, it can be time consuming due to the duration of image acquisition (fine material necessitates high resolution images), and the post-processing of the SEM images required to make them suitable for quantitative analysis. There is also an assumption of shape required to convert from 2D images to a GSD in terms of volume %.

Other image analysis methods use optical imagery. For example, the Morphologi G3 particle analyser by Malvern Panalytical scans and rapidly images particles that have been dispersed onto a glass plate; size and shape are measured using the built-in software. One constraint of this method for GSD determination, however, is that the sample must be sieved prior to analysis to ensure optimal particle dispersion and image resolution (Leibrandt and Le Pennec 2015; Buckland et al. 2018; Freret-Lorgeril et al. 2019). Studies of cryptotephra (non-visible tephra layers) also quantify grain size using optical imaging methods; size is typically measured along the longest particle axis (e.g., Palais et al. 1992; Zdanowicz et al. 1999; Stevenson et al. 2015). Here chemical and physical tephra extraction (Dugmore and Newton 1992; Cooper et al. 2019) is required before tephra shards are counted and imaged using an optical microscope. However, part of the tephra extraction process involves removing very fine material by wet sieving (<20 µm) and only a small number of particles are measured (~100; Stevenson et al. 2015). These aspects of the sample handling, combined with the different size parameterisation, make cryptotephra GSDs difficult to compare with GSDs from other methods (Cashman and Rust 2020).

2.2.6. In situ methods

In situ methods of particle size analysis utilise a variety of the measurement principles used by laboratory methods such as diffraction and image analysis (Table 1). As with laboratory methods of size analysis, the grain size range and definition of size is unique to each in situ method and instrument. Ground-based radar systems such as the PLUDIX instrument (Scollo et al. 2005; Bonadonna et al. 2011) measure the settling velocity of particles from ~1 – 10 mm. The settling velocity is converted into a PSD by assuming spheres with variable densities (Bonadonna et al. 2011); thus size is quantified as an equivalent sphere diameter. Optical disdrometers, such as the Parsivel^2, also quantify size as the volume equivalent sphere diameter according to the manufacturers specifications (Kozono et al. 2019; OTT 2020), however, studies of rainfall found that the measured size of non-spherical particles is closer to the maximum horizontal diameter (Table 1; Adachi et al. 2013). In situ high resolution 2D imaging of active tephra fall can measure particles from ~0.0625 - 2 mm; the images can be used to determine multiple size descriptors including minimum and maximum particle lengths and area equivalent measures (Miwa et al. 2020). Finally, the methods used to determine PSDs from satellite infrared measurements typically assume that the particles are dense spheres with a constant refractive index and that the scattering can be resolved using Mie theory; thus the ‘size’ reported refers to a sphere diameter (Wen and Rose 1994; Pavolonis et al. 2013; Kylling et al. 2014; Stevenson et al. 2015). Note that the term ‘effective radius’ that is used in remote sensing refers to a log-normal PSD that contains a range of particle sizes rather than a single particle size (Stevenson et al. 2015).

2.2.7. Grain size statistics

After the GSD of tephra has been measured using the techniques described above, the convention is to report GSD statistics that facilitate comparison with other distributions. The most common parameters reported for volcanic GSDs are based on the Inman (1952) or Folk and Ward (1957) graphical methods which determine the mean (μ), median (Md), standard deviation or sorting (σ), skewness (Sk) and Kurtosis (K; Blott and Pye 2001). These methods were designed for grain size data on the φ-scale and require very little data manipulation (Appendix A). This method, however, assumes that the GSD follows a log-normal distribution, in other words the GSD is normally distributed on the φ-scale. Alternatively, the GSD can be described using a Weibull or Rosin-Rammler distribution (Rosin and Rammler 1933; Weibull 1951; Brown and Wohletz 1995) from which shape and scale parameters can be described (Appendix A). Log-normal and Weibull distributions can be fit as mixture models to account for the multimodal form of many volcanic GSDs (Appendix A; Eychenne et al. 2012, 2015; Costa et al. 2016; Pioli et al. 2019; Mele et al. 2020). The number and proportion of subpopulations provide additional parameters that can be compared between different samples and in some cases subpopulations can be related to distinct eruptive processes (e.g., Sheridan 1971; Eychenne et al. 2012, 2015).

Common themes found when reviewing grain size methodologies (Table 1) are the lack of quantified shape characterisation, the need to assume particle properties such as density and refractive index (sieving, sedimentation, laser diffraction and electrozone sensing), and slow data collection (SEM image analysis and the pre-analysis sample preparation required for any method). Furthermore, the amount of material analysed varies between methods. Notably, the Mastersizer 3000, Morphologi G3 and SEM image analysis use <10 mg of material per analysis, which can cause undercounting of large grains. Hence the rationale for developing approaches to particle size analysis that no do not require assumptions of shape and the pertinence of methods that can measure multiple size parameters for non-spherical particles.

3. Methods

3.1. Instrumentation

Here we present a relatively new analytical approach to characterise the size and shape of tephra which addresses some of the limitations of other techniques. The protocol involves the CAMSIZER® X2 (CX2), a particle analyser manufactured by Microtrac MRB (formerly Retsch Technology) that utilises dynamic image analysis (DIA; ISO 13322-2) to characterise the grain size of particulate materials. Castro and Andronico (2008) published a detailed INGV report outlining similar procedures using an earlier CAMSIZER model, although the CX2 model described in this study has capabilities to work with much finer material (>0.8 µm) thanks to the multiple particle dispersion modules.

3.1.1. Basic functions of the CX2

The CX2 is a compact particle analyser that consists of three key components: the sample feeder and particle dispersal module, the imaging module, and a desktop computer running the CX2 software (Fig. 1). The DIA principle requires that particles are dispersed past the field of view of two high resolution digital cameras to image the moving particles that are back lit by an LED (Fig. 1). The combination of two cameras (one basic and one zoom) ensures that a range of particle sizes (0.8 µm – 8 mm) can be imaged at an optimum resolution. These images are processed in real-time by the CX2 software to generate shape and size distributions and compute grain size statistics.

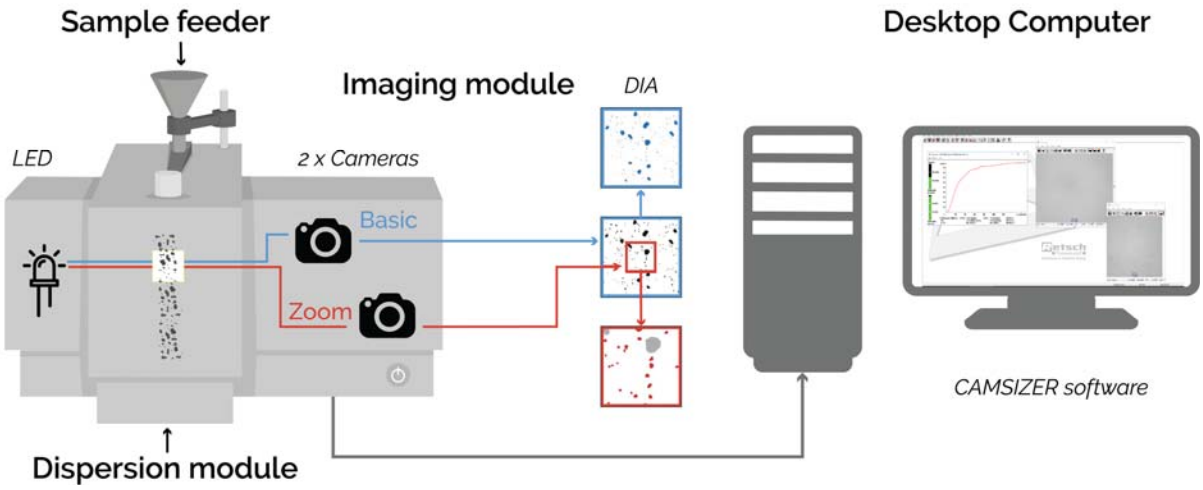

Figure 1 – Modular set up of CAMSIZER® X2 modified from MicroTrac MRB (2020).

The particles are dispersed past the cameras' field of view by one of three mechanisms: wet dispersion (X-wet), compressed air (X-jet) or as free-falling particles (X-fall). Each dispersion mechanism has an optimum grain size range. The X-fall dispersion is best for coarse material (10 µm to 8 mm), X-jet covers 0.8 µm – 5 mm and X-wet is suited to fine material (0.8 µm – 1 mm). The choice between X-jet and X-wet for fine material (0.8 µm – 1 mm) depends on the maximum grain size and amount of material available to be analysed. The X-wet uses only a very small amount (<10 mg) of material for analysis so is best suited to volume-limited fine-grained samples. The choice of dispersion method for coarse material (5 - 8 mm) depends on whether sample recovery is required, which is only possible for the X-fall.

For every analysis, the CX2 requires a 'task file' (Castro and Andronico 2008) that informs the software of the analytical conditions to use and allows the user to customise the data acquisition. For example, particles with certain characteristics (e.g. related to size or shape parameters) can be excluded; this is useful for eliminating contaminating fibres which have extreme values of shape parameters such as compactness and convexity (Table 2). One important feature of the task file is whether a 'velocity adaption' is required. When using the X-fall module (free falling particles), a correction is needed to account for large particles falling faster than small particles under gravity, which causes them to be undercounted as they remain in the field of view of the camera for less time. In contrast, the X-jet dispersion mechanism requires the software to correct for small particles moving faster in the stream of compressed air relative to large particles. The user generates the velocity adaption within the CX2 software by producing a calibration curve of particle size versus particle velocity. Best practise is to produce a new velocity adaption for samples where there is a broad GSD, and for samples that have not been analysed using the CX2 before (i.e. where there no pre-existing task file).

Table 2 – Size and shape parameters used by the CAMSIZER® X2 software

Notation or symbol	Name	Definition or formula	Alternative nomenclature
A_P	Area of particle		
A_{CH}	Area of bounding convex hull		
U	Perimeter		
r_1 and r_2	Particle radii	Minimum and maximum radii of a particle from the centre of the particle area	
xarea	Equivalent circle diameter	Diameter of the circle having the same projection area of the particle	
x_{Fe}	Feret diameter	The perpendicular distance between parallel tangents touching opposite sides of the profile	Length, caliper diameter
$x_c min$	Chord diameter	Minimum width of the particle	Width, minimum rope
x_{Ma}	Martin diameter	Line bisecting the area of the particle	
SPHT	Sphericity	$\frac{4\pi A_P}{U^2}$	Form factor (Liu et al. 2015)
b/l	Aspect ratio	$\frac{x_c min}{x_{Fe} max}$	Width to length ratio, axial ratio (Liu et al. 2015)
CVX	Convexity	$\frac{A_P}{A_{CH}}$	Solidity (Liu et al. 2015), roughness
CPT	Compactness	$\frac{\sqrt{\frac{4A_P}{\pi}}}{x_{Fe} max}$	Roundness (Liu et al. 2015)
Symm	Symmetry	$\frac{1}{2}\left[1 + \min\left(\frac{r_1}{r_2}\right)\right]$	

3.1.2. Principles of dynamic image analysis

The raw images captured by the basic and zoom cameras are converted to binary images (particle versus no particle). The size and shape of the particles in each image are measured by the CX2 software using an algorithm that combines the results from the basic and zoom cameras. Every particle above a minimum size threshold is measured, with the minimum size determined by the limit of image resolution or the limit set in the task file. The software has the capacity to measure 100's of millions of particles at >300 images per second, and can measure multiple size and shape parameters per particle (Table 2; MicroTrac MRB 2020). Three key size parameters are equivalent circle diameter (xarea), minimum chord diameter ($x_c$min) and maximum Feret diameter (x_{Fe}max; Table 2; Fig. 2). These parameters are not identical for irregular particles and therefore yield different information about the particle distribution. Importantly, computing all three size parameters allows CX2 outputs to be compared with different grain size measurement methods. For example, laser diffraction using Mie theory outputs equivalent sphere diameters (~xarea) while cryptotephra data report the long axis (x_{Fe}max) and the retaining sieve aperture should be greater than or equal to the minimum diameter of a particle ($x_c$min; Freret-Lorgeril et al. 2019).

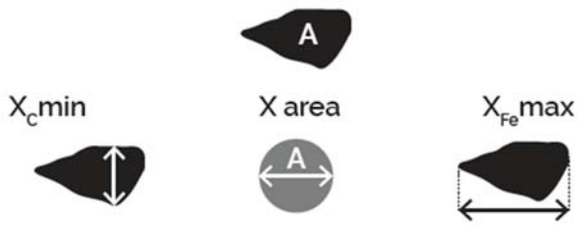

Figure 2 – Schematic of three key size parameters; $x_c$min the minimum chord diameter, xarea the equivalent circle diameter and x_{Fe}max the maximum Feret diameter.

To obtain a GSD using the CX2, the results of the 2D image analysis are converted to 3D by calculating an apparent volume per particle. The conversion from area to volume depends on the size parameters chosen. Using xarea, the conversion to volume assumes spherical particles, whereas using x_{Fe}max and $x_c$min assumes ellipses where the long and short axes are represented by x_{Fe}max and $x_c$min respectively

(Castro and Andronico 2008). The data can be output as a GSD in terms of volume fraction or as a particle number distribution (PND; number of particles in each size fraction).

3.1.3. Post-processing and data analysis

The CX2 software has flexible data processing that allows adjustable binning of raw data (logarithmic or arithmetic). This means that there are no restrictions equivalent to those that arise from fixed sieve intervals. The software outputs the GSD as a probability density function and cumulative distribution function (PDF and CDF), and has customisable data visualisation options. The output of the CX2 software is a 'resource description framework' file (.rdf), that can be output as a Microsoft Excel compatible file (.xle) for user-specific data processing and analysis. Images can also be saved.

Another useful feature in the CX2 software is the 'particle wizard' tool, which crops the saved images to allow visualisation of individual particles. This can be helpful for ensuring the task file has been designed correctly. For example, particles with specific shape and size characteristics can be displayed to confirm that contaminants (such as fibres) are identified and eliminated from the GSD. The particle wizard is also useful for qualitatively characterising particle shapes in different size fractions.

To facilitate flexible and reproducible data processing and visualisation, we analyse sample GSDs in Microsoft Excel and R. We output each GSD from the CX2 in two grain size bin configurations, one equivalent to a quarter-φ scale for compatibility with sieve data, and one on the linear scale with a bin width of 5 μm. For all GSDs we compute the Folk and Ward (1957) graphical parameters of mean (μ_{FW}), standard deviation or sorting (σ_{FW}), skewness (Sk) and Kurtosis (K). We also fit log-normal and Weibull distributions directly to the GSDs using the 'fitdistrplus' package in R (Delignette-Muller and Dutang 2015). Mixture models of log-normal and Weibull distributions were fit to multimodal GSDs using the 'mixfit' function from the 'mixR' R package (Yu 2018). The probability density functions, and distribution fitting methods are reported in Appendix A.

3.2. Test samples and method comparison

3.2.1. Sample preparation and data collection

To test the capabilities and performance of the CX2, we conducted a series of preliminary analyses with glass spheres (ballotine) and natural samples that had been characterised using other techniques. Prior to analysis, some sample preparation was required. To gauge the approximate size, the ballotine were dry sieved into 6 sieve fractions using disposable nylon sieve meshes to ensure no contamination: >500 µm, 355 – 500 µm, 100 – 250 µm, 65 – 110 µm, 50 – 65 µm and 20 – 50 µm. The natural samples include Mazama tephra (~ 7.7 ka eruption of Crater Lake, OR, USA) sampled at different distances from source (Buckland et al. 2020), hydromagmatic fallout samples from the Hverfjall Fires (~2.5 ka eruptive episode of Krafla Volcanic System, Iceland) sampled by Liu et al. (2017), Campanian Ignimbrite tephra (~39 ka eruption from Phlegrean Fields, Italy) sampled by Engwell et al. (2014), and tephra from the 1980 eruption of Mount St Helens (MSH), Washington, USA sampled via multiple sources (Meredith 2019). Some of the MSH samples are assumed to be equivalent to samples analysed by other authors (Sarna-Wojcicki et al. 1983; Durant et al. 2009) based on comparable sampling locations (Supplementary S1). The tephra was dried to eliminate particle cohesion (Castro and Andronico 2008) and dry sieved into half-φ intervals from 8 mm - 125 µm (-3 to 3 φ) where necessary. Further information on the natural samples can be found in the supplementary information.

3.2.2. Choice of size parameters

To explore the reliability of the different size parameters calculated by the CX2, we measured the ballotine sieve fractions using xarea, x_{Fe}max and $x_c$min (Fig. 2). As expected, the choice of size parameter for the ballotine did not significantly alter the GSD in any sieve fraction (Fig. 3a) because xarea, x_{Fe}max and $x_c$min are equal for spherical particles (equivalent to circular in 2D images; Fig. 3c). The near vertical cumulative distributions reflect the manufacturing of the ballotine to achieve similar sizes. There is a slight fine tail in two of the analyses (Fig. 3a) that could indicate imperfect sieving where the finer material hadn't fully segregated into the correct sieve fraction. The largest variability in size parameter is observed in the x_{Fe}max data. This is attributed to the presence of slightly elongated spheres which we observed with optical microscope images (Fig. 3b). Similarly, the coarsest sieve fraction contained some irregular particles (Fig. 3c), which are likely a manufacturing fault.

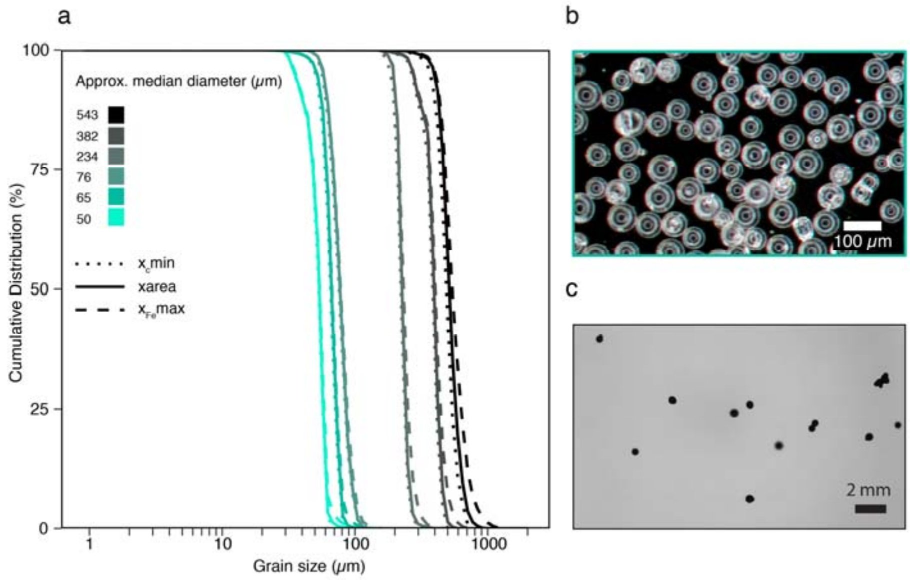

Figure 3 – Comparing the size parameters for six ballotine size fractions. a) Cumulative grain size distributions showing that the three size parameters (differentiated by the line pattern) plot close to on top of each other for each size fraction (differentiated by the line colour). b) Optical microscope image of the 65 – 110 μm sieve fraction. c) CX2 image from the DIA of the >500 μm sieve fraction.

We repeated this analysis on the sieved Mazama and Campanian samples to further explore the sensitivity of GSDs to size parameter (Fig. 4). Irregular particles, such as volcanic tephra, have GSDs that vary within a sieve fraction according to the size parameter. Parameter $x_c$min is best suited for combining sieve analysis and DIA (Fig. 4b) because the $x_c$min GSD falls within the expected sieve range according to sieve diameter *d*. Extending the sieve range so that the maximum grain size is equal to the hypotenuse of the sieve aperture shows better agreement with the xarea GSD (Fig. 4b) consistent with comparisons between optical image analysis (Morphologi GS3) and sieving (Freret-Lorgeril et al. 2019). In contrast, the coarse tail on the x_{Fe}max GSD extends well beyond both sieve ranges, indicating that elongated particles can pass through the sieves on their intermediate or short axes. The xarea and x_{Fe}max distributions within a size fraction also vary between samples (Fig. 4). For example, the median x_{Fe}max of the Campanian 2φ sieve fraction is 512 μm, compared to a median x_{Fe}max of 427 μm for the same sieve fraction of Mazama tephra. Similar to the ballotine analyses (Fig. 3), all GSDs have fine tails below the sieve range signifying that fine material is often retained in coarse sieves due to imperfect segregation as a result of the aggregation of fines or the adhesion of fine material to larger particles.

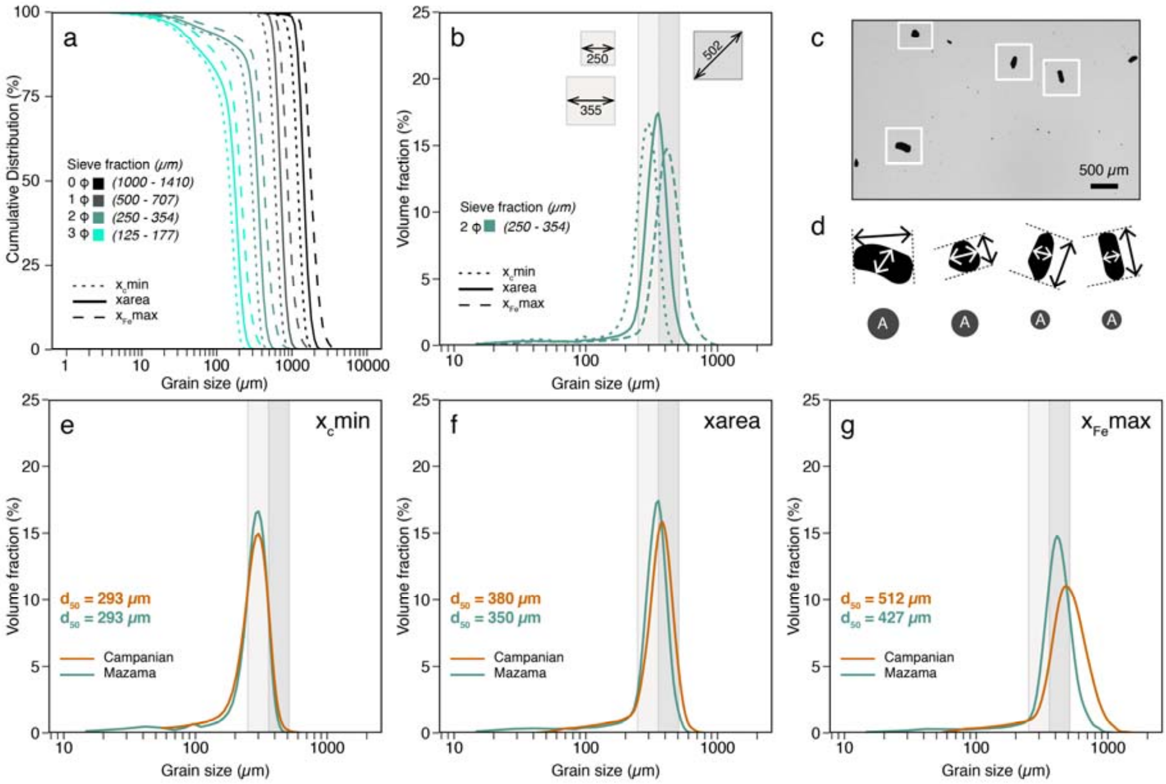

Figure 4 – Comparing different size parameters for natural sieved tephras. a) Cumulative GSDs for Mazama tephra showing the three size parameters (differentiated by the line pattern) for each half-φ sieve fraction (differentiated by the line colour). b) GSDs of the 2 φ (250-354 μm) sieve fraction for each size parameter. The light grey box indicates the size range expected from sieving according to sieve diameter, *d*; the dark grey box extends this range to the length of the sieve aperture hypotenuse. c) CX2 image from the DIA (using X-Jet) of the 2 φ sieve fraction of Mazama tephra. d) Binary images of irregular Mazama tephra particles from c) with $x_{Fe}max$, x_cmin and xarea indicated. e-g) Comparing GSDs within a sieve fraction according to the size parameter for the Mazama and Campanian Ignimbrite tephras.

3.2.3. Shape parameters and distributions

The CX2 measures multiple shape parameters. Three shape parameters measured on the ballotine and natural samples were sphericity (SPHT; $\frac{4\pi A_P}{U^2}$), symmetry (Symm; $\frac{1}{2}\left[1+\min\left(\frac{r_1}{r_2}\right)\right]$) and aspect ratio (b/l; Table 2; Fig. 5). For perfectly spherical particles these parameters should equal 1 for all grain sizes. However, small imperfections and deviations from perfect spheres will reduce these shape parameters to <1 and each has a different sensitivity. For example, the interpretation that the $x_{Fe}max$ results (Fig. 3) for the coarser ballotine contained a larger proportion of non-spherical particles is supported by the lower values of both symmetry and aspect ratio (Figs. 5 b&c). In contrast, the coarsest ballotine has a higher median SPHT than the finest ballotine and there is no significant change in the range of SPHT values with grain size (Fig. 5a). SPHT (Fig. 5a) is particularly sensitive to particle perimeter so is lower for particles with high surface roughness; the generally smooth perimeters of the ballotine thus suggests that deviations from perfect spheres arise primarily from elongation and surface protrusions rather than surface roughness (Fig. 3c).

Shape data are also susceptible to differences in image resolution, which becomes a problem when samples span a wide size range (e.g. Saxby et al. 2020). For example, the high number of pixels per particle for coarse particles could increase the particle perimeter measurement relative to the particle area, which would artificially lower the SPHT. Nevertheless, our data on ballotine show little relation between particle size and the SPHT (Fig. 5a) and we attribute the changes in Symm and b/l with grain size to imperfections in the ballotine (Fig. 3) rather than differences in image resolution.

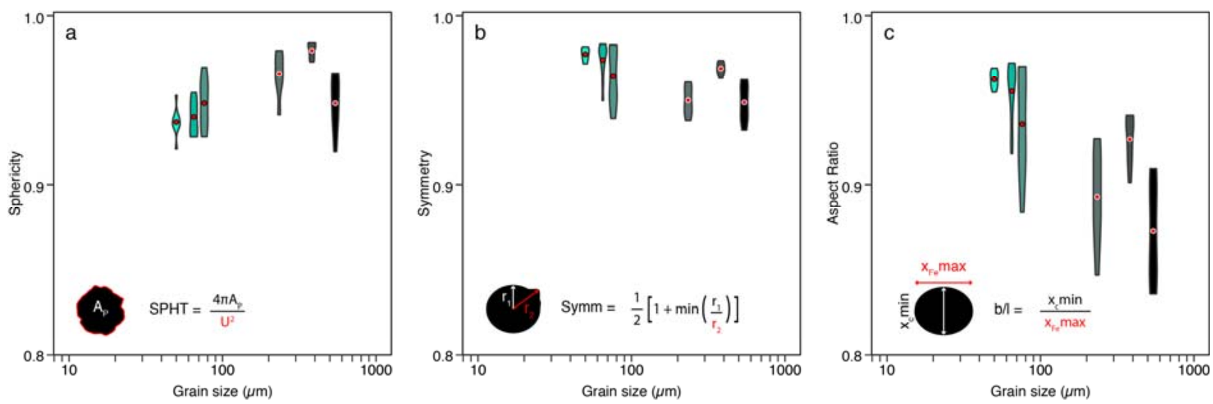

Figure 5 – Shape parameters indicating the deviation of ballotine from perfect spheres. Violin plots show the distribution of the shape parameters for the median grain size. The red dot corresponds to the mean value of the shape parameter. a) Sphericity (SPHT), b) Symmetry (Symm) and c) Aspect ratio (b/l).

It is evident from the shape distributions measured for the natural tephra samples that the CX2 can be used to differentiate samples according to particle shape (Fig. 6). Compared to the ballotine, the distribution of SPHT values for the sieved Campanian Ignimbrite, Hverfjall and Mazama tephras show a wide range of SPHT values as a result of the irregular particle morphology (Fig. 6a). The Mazama distribution shows the highest SPHT values as it contains a high proportion of free crystals with smooth surface textures compared to the basaltic Hverfjall and micro-pumice rich Campanian Ignimbrite tephras (Fig. 6a). Interestingly, bimodal MSH samples display a different SPHT distribution relative to the unimodal samples (Fig. 6b); here bimodal samples have been interpreted to record particles produced by different phases of the eruption (Eychenne et al. 2015). The aspect ratio (b/l), which reflects the elongation of particles, is lowest for the Campanian Ignimbrite tephra but shows no real difference between the Hverfjall and Mazama tephras (Fig. 6c).

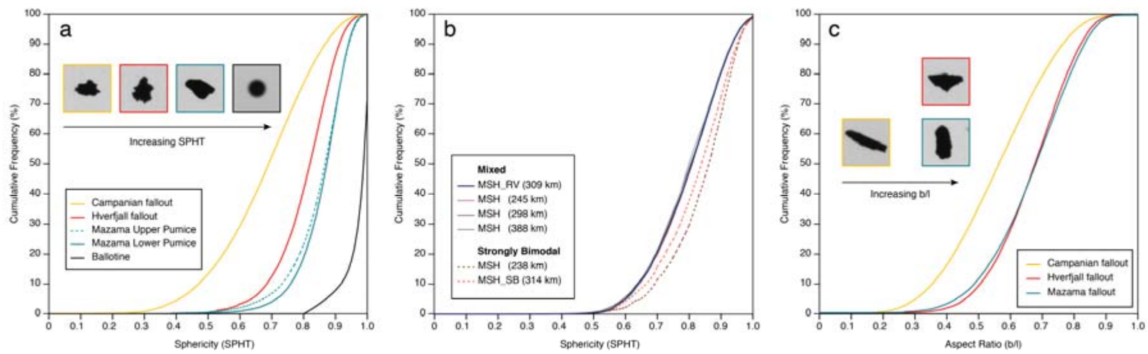

Figure 6 – Cumulative shape distributions for ballotine and natural samples. a) Comparing SPHT for individual sieve fractions of ballotine and natural tephra samples. The 2.5 φ sieve fraction (180-250 µm) is shown for the natural samples, and the ballotine data is for the sieve fraction with 234 µm median diameter. b) SPHT distributions for distal MSH samples. c) Comparing b/l distributions for the 2.5 φ sieve fraction of natural tephra samples.

3.2.4. Comparison of CAMSIZER X2 results with other methods

The GSD of the natural samples has been previously characterised using a combination of sieving and laser diffraction (Mt. St. Helens, Durant et al. 2009; Campanian Ignimbrite, Engwell et al. 2014;

Hverfjall Fires, Liu et al. 2017; Mazama, Buckland et al. 2020). Here we compare the GSDs of fine-grained tephras measured using laser diffraction with GSDs measured using DIA with X-jet and X-flow dispersion mechanisms (Fig. 7). The laser diffraction GSDs have a broader fine-grained tail than the CX2 results (Fig. 7). For example, laser diffraction suggests that 10% of the volume of the MSH tephra is <4 μm compared to the X-jet GSD which suggests that 10% of the sample is <8 μm (Fig. 7b). X-jet and X-wet GSDs also differ slightly at the coarse end of the distribution with the X-flow distribution showing that <5% of the Mazama tephra is coarser than 100 μm while the laser diffraction and X-jet distributions show that >10% of the sample is coarser than 100 μm (Fig. 7a). We expect the xarea GSDs to be the most comparable to GSDs from laser diffraction if Mie scattering theory is used (Fig. 7a-b). The Campanian Ignimbrite GSD measured by laser diffraction used the Fraunhofer approximation and appears to be best matched by x_{Fe}max in the CX2 GSD (Fig. 7c).

The differences at the <10 μm end of the scale between the CX2 and laser diffraction are due to the different minimum particle sizes measured by the instruments. Laser diffraction detects particles >0.01 μm, whereas the lower size limit of the CX2 is 0.8 μm. For very fine-grained material (<10 μm) there are also some limitations of laser diffraction. For example, fine material can cause multiple scatterings of the laser beam, and some authors have attributed an overestimation of fine particles to the presence of non-spherical grains (Vriend and Prins 2005; Jonkers et al. 2009). The differences in the GSDs >100 μm are likely the result of the amount of material analysed. The X-jet method analyses the largest quantity of material (>10 mg) which ensures representative sampling of the coarse particles unlike the wet dispersion methods which use <10 mg of material.

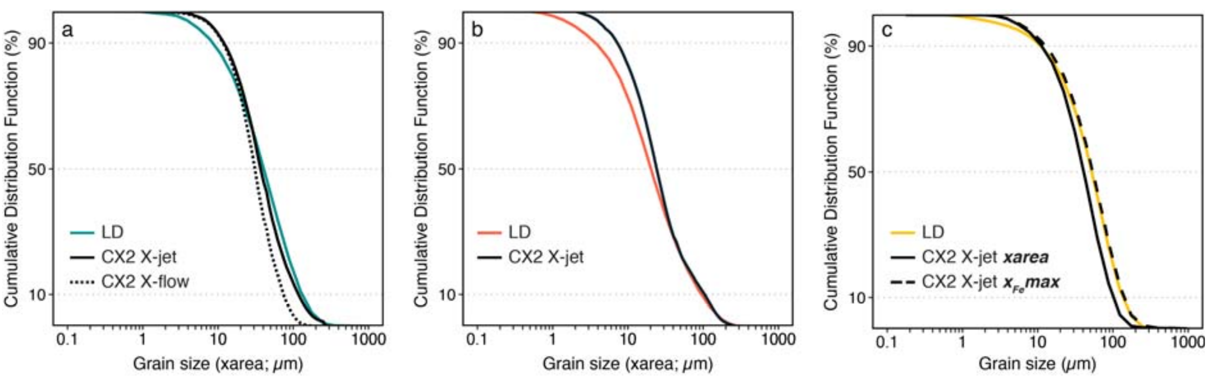

Figure 7 – Comparing GSDs from laser diffraction (LD) with CX2 GSDs for fine-grained distal tephras. a) GSDs for distal Mazama sample from site 73. b) GSDs for distal MSH sample. Laser diffraction analysis carried out on sample DAVIS11 by Durant et al. (2009), corresponding sample MSH_RV analysed using CX2 for this study (see Supplementary S1). c) GSDs for ultra-distal Campanian Ignimbrite tephra. Laser diffraction analysis from Engwell et al. (2014) compared to X-jet GSDs according to size parameter.

For the coarser Mazama tephra, we compare GSDs measured using a combination of sieving and CX2 (X-jet) with GSDs produced using the CX2 alone, where the X-fall (>125 μm) and X-jet analyses are combined (<125 μm, Fig. 7). The sieving and CX2 data were combined using the overlap between the methods at 125 - 250 μm by assuming a constant density and therefore converting the volumetric size distribution (CX2) to a mass distribution (e.g. Eychenne et al. 2012). The X-fall and X-jet data were combined by weighting the coarse and fine distributions according to the mass percentage that was greater than and less than 125 μm. For the sake of comparison, all data were processed in half-φ intervals to match the limits of data manipulation imposed by sieving.

The difference between the GSDs in Figure 8 results from the distinction between coarse GSDs that are quantified as weight percent (mass%; sieving & CX2) versus volume percent (vol%; CX2). The GSDs from sieving have a strong mode at 2 – 1.5 φ (250 – 354 μm), which corresponds to the sieve fraction that contains a large proportion of dense phenocrysts (magnetite and pyroxene); this mode remains constant throughout the Mazama tephra section (upper and lower pumice fallout units, see Supplementary S1). The modes in the CX2-only distributions (Fig. 8) do not align with the GSDs from sieving because they are represented in terms of the vol% (rather than mass%) in each size class. This means that although the X-fall and X-jet analyses are combined by the relative mass% > and <125 μm, dense individual size fractions (crystal concentrations) do not manifest as the mode of the GSDs.

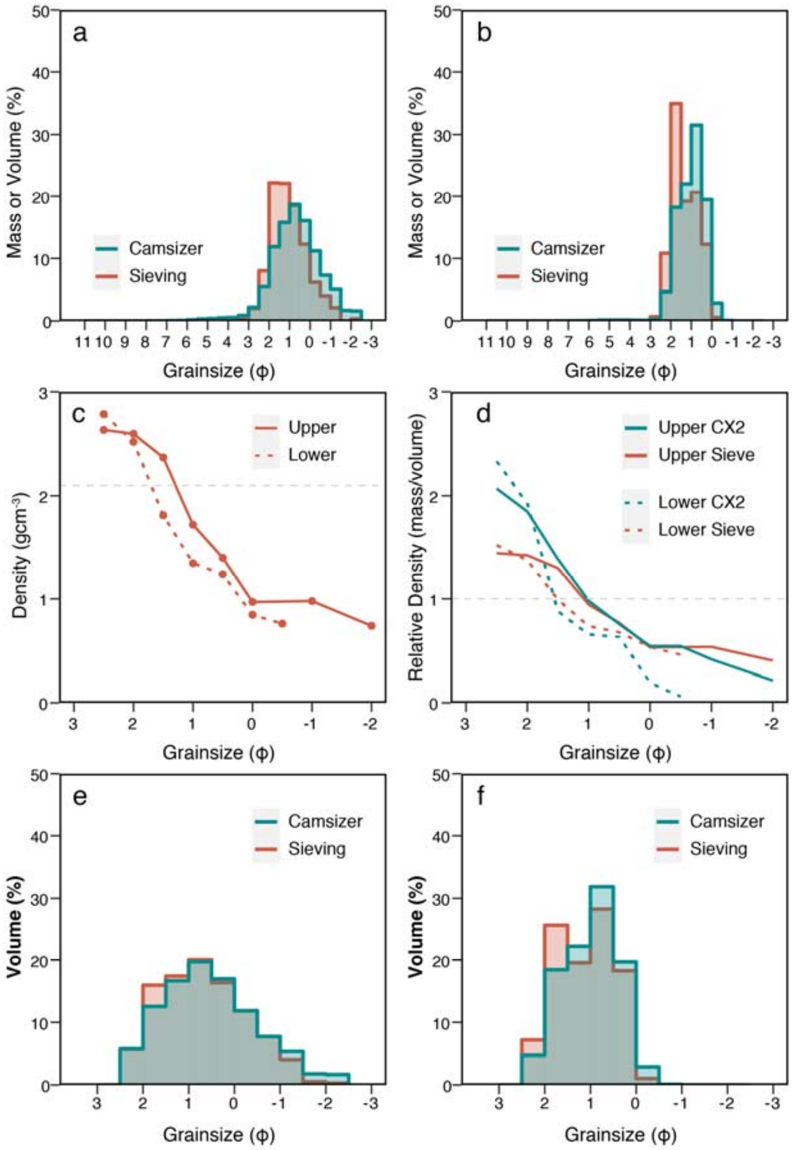

Figure 8 – Comparing GSDs of Mazama tephra measured by sieving & CX2, with CX2 alone. All samples are from a fallout section located at site 46 ~120 km from source (see supplementary information S1). a) Sample from the upper pumice unit, b) sample from the lower pumice unit. c) Measured densities (gcm^{-3}) of individual sieve fractions for the upper and lower unit with the dashed line indicating the density of Mazama glass ~2.1 gcm^{-3}. d) The relative density of half-φ sieve fractions calculated using the sieve data (red) and the CX2 & sieve data (blue). e) and f) Comparing the volume distributions measured using the CX2 with calculated volume distributions from sieve data for the upper (e) and lower (f) units between 2.5 and -2.5 φ.

4. Results

The method development and testing (section 3) shows that the CX2 provides an appropriate analytical protocol for characterising the grain size and morphology of volcanic tephra. Here we explore the unique capabilities of DIA for determining accurate GSDs of samples with non-uniform density distributions and then examine the sensitivity of grain size statistics to the choice of size parameter and method of grain size measurement.

4.1. Non-uniform density distributions

The CX2 and sieve analyses of the coarse Mazama tephra (Fig. 8) differ because of the non-uniform density of the pyroclasts across the GSD (Fig. 8), in contrast to parallel sieve and CX2 analyses of natural tephras with less significant changes in clast density that show similar GSDs when quantified by either mass or volume (Supplementary S2). This contrast suggests we can use simultaneous measurements of GSDs by mass and volume to invert for density distributions.

To obtain independent measurements of density, we used a water pycnometer (e.g. Eychenne and Le Pennec 2012; Liu et al. 2017) to analyse the -2 and 2.5 φ sieved size fractions of Mazama samples from the upper and lower pumice units (Fig. 8c). These data show the expected increase in particle density with decreasing size (Bonadonna and Phillips 2003; Eychenne and Le Pennec 2012) and highlight the high density ($\rho \sim 2.6$ gcm^{-3}) of the 2 and 2.5 φ sieve fractions where pyroxene and magnetite crystals are concentrated, a density that greatly exceeds that of the matrix glass (~2.1 gcm^{-3}). We used the sieved mass and measured density of each size class to calculate a volume-based GSD to compare with the CX2 GSD (Fig. 8e-f). This comparison shows that relative to the sieve data, the CX2 underestimates the volume in the densest sieve fraction (2.5 φ) and overestimates the volume of the coarse pumice clasts. This is reflected in the values of relative density calculated by dividing the mass % by the volume % in each class using both the sieve data and CX2 data (Fig. 8d). Importantly, whilst the resulting absolute values of relative density are incorrect, the relative density profiles derived from the CX2 data do emphasize the dense crystal rich grain size fractions (3 – 1.5 φ) relative to the coarse low-density pumice clasts (<1.5 φ), suggesting that a direct comparison of mass and volume provides important information about the particle population.

4.2. Grain size distribution statistics

Grain size statistics provide a way to quantitatively compare GSDs that arise from different measurement methods. For example, the Folk and Ward (FW;1957) mean grain size (μ_{FW}) calculated for the Mazama upper pumice is 1.07 φ (476 µm) for sieve data compared to 0.38 φ (768 µm) for the CX2 GSD (Table 3). Similarly, for fine-grained Mazama samples (Fig. 7), μ_{FW} varies from 4.73 – 5.38 φ (38 – 24 µm) depending on the size parameter ($x_c$min or xarea) and method of grain size analysis used (laser diffraction or CX2; Table 3). The FW sorting (σ_{FW}; measure of spread) and skewness (Sk; measure of symmetry) also depend on the method used (Table 2). For example, the Sk of the lower pumice is -0.20 when measured by sieving but +0.15 when measured with the CX2. This difference affects the qualitative classification from finely skewed (sieving) to coarsely skewed (CX2; Table A1). Another important parameter is the proportion of fine (<125 µm) and very fine (<15 µm) ash. Here the proportion of very fine ash (<15 µm) in sample MZ73 ranges from 16 % (xarea; X-jet) to 26% ($x_c$min; X-wet) of the total volume.

The statistics and interpretation of multimodal GSDs are similarly sensitive to the method used to characterise the distribution (Fig. 9; Table 4). The distal MSH ash has previously been shown to contain at least two grain size sub-populations (Durant et al. 2009; Eychenne et al. 2015). Deconvolution of GSDs into subpopulations, however, is sensitive to both differences in the starting GSD and the distribution chosen (log-normal or Weibull; Appendix A), as illustrated by PDFs deconvolved for the laser diffraction GSD compared to the CX2 GSD. When the number of log-normal subpopulations is fixed at 2, the laser diffraction GSD (Fig. 9a) is resolved into distributions with means of 9.23 φ (2 µm) and 5.47 φ (26 µm). The same fitting algorithm applied to the CX2 GSD resolves two sub-populations with means of ~5.6 and 3.0 φ (21 and 125 µm) respectively (Fig. 9b; Table 4). This comparison shows that two samples from the same deposit, taken from the same location, can have GSDs that can be interpreted differently simply because of measurement method.

It is well known that grain size statistics are sensitive to the bin size. To explore this sensitivity we processed the data in multiple bin configurations (Table 4). We find that fitting of unimodal and bimodal distributions is not strongly affected by the type of binning used, particularly when working with fine-grained material (e.g., Fig. 9f). However, coarse bins are still problematic for particles >500 µm when using the φ-scale as this translates into a wide range on the linear scale and poor resolution of the distribution within the sieve intervals (Hails et al. 1973). Similarly, coarse linear binning (>5 µm) can obscure the GSD in the fine grain sizes and places too much emphasis on the coarse particles (Blott and Pye 2001).

Table 3 – Grain size statistics calculated for different methods of grain size analysis.

Sample	Method	Binning	μ_{FW} (φ)	σ_{FW} (φ)	Sk_{FW}	<125 µm (%)	< 15 µm (%)
MZ46 Upper Pumice *(Fig. 8a)*	Sieving & CX2	½ φ	1.07	0.92	-0.15 *(coarse skewed)*	2.4	0.2
	CX2 *($x_c$min)*	½ φ	0.66	1.15	-0.04 *(symmetrical)*	2.4	0.2
MZ46 Lower Pumice *(Fig. 8b)*	Sieving & CX2	½ φ	1.32	0.67	-0.20 *(coarse skewed)*	0.82	0.01
	CX2 *($x_c$min)*	½ φ	1.00	0.65	0.13 *(fine skewed)*	0.84	0.01
MZ73 *(Fig. 7b)*	CX2 X-jet *($x_c$min)*	¼ φ	5.11	1.24	-0.01 *(symmetrical)*	95	23
	CX2 X-jet *(xarea)*	¼ φ	4.74	1.27	-0.01 *(symmetrical)*	91	16
	CX2 X-wet *($x_c$min)*	¼ φ	5.38	1.01	0.06 *(symmetrical)*	99	26
	CX2 X-wet *(xarea)*	¼ φ	5.03	1.04	0.05 *(symmetrical)*	99	17

LD *(xarea)*	$^{1}/_{2}$ φ	4.73	1.53	0.139	89	20

*FW = Folk and Ward (1957) graphical method of calculating GSD statistics.

Table 4 – Main parameters of bi-modal MSH samples calculated using different methods of grain size analysis and different bin configurations. $\mu_{\varphi 1}$, $\mu_{\varphi 1}$ = log-mean, $\sigma_{\varphi 1}$, $\sigma_{\varphi 2}$ = log-standard deviation, p_1, p_2 = proportion of the total GSD of the fine- and coarse-grained subpopulations respectively.

Sample	Method	Binning	$\mu_{\varphi 1}$	$\mu_{\varphi 2}$	$\sigma_{\varphi 1}$	$\sigma_{\varphi 2}$	p_1	p_2
DAVIS11*	LD	$^{1}/_{2}$ φ	9.23	5.47	0.83	1.56	0.06	0.94
MSH_RV	CX2 *(xarea)*	$^{1}/_{2}$ φ	5.53	2.92	1.28	0.43	0.92	0.08
	CX2 *($x_c$min)*	$^{1}/_{2}$ φ	5.76	3.13	1.28	0.46	0.92	0.08
MSH_SB	CX2 *($x_c$min)*	1 φ	5.92	3.42	1.35	0.50	0.75	0.25
		$^{1}/_{2}$ φ	5.93	3.34	1.27	0.37	0.75	0.25
		$^{1}/_{4}$ φ	5.93	3.34	1.25	0.32	0.74	0.26
		1 μm	5.94	3.36	1.25	0.32	0.75	0.25
		5 μm	5.92	3.33	1.35	0.31	0.76	0.24
		10 μm	5.94	3.32	1.45	0.31	0.76	0.24

* DAVIS 11 sample was sampled very close to MSH_SB (Sarna-Wojcicki et al. 1981; Durant et al. 2009; Meredith 2019)

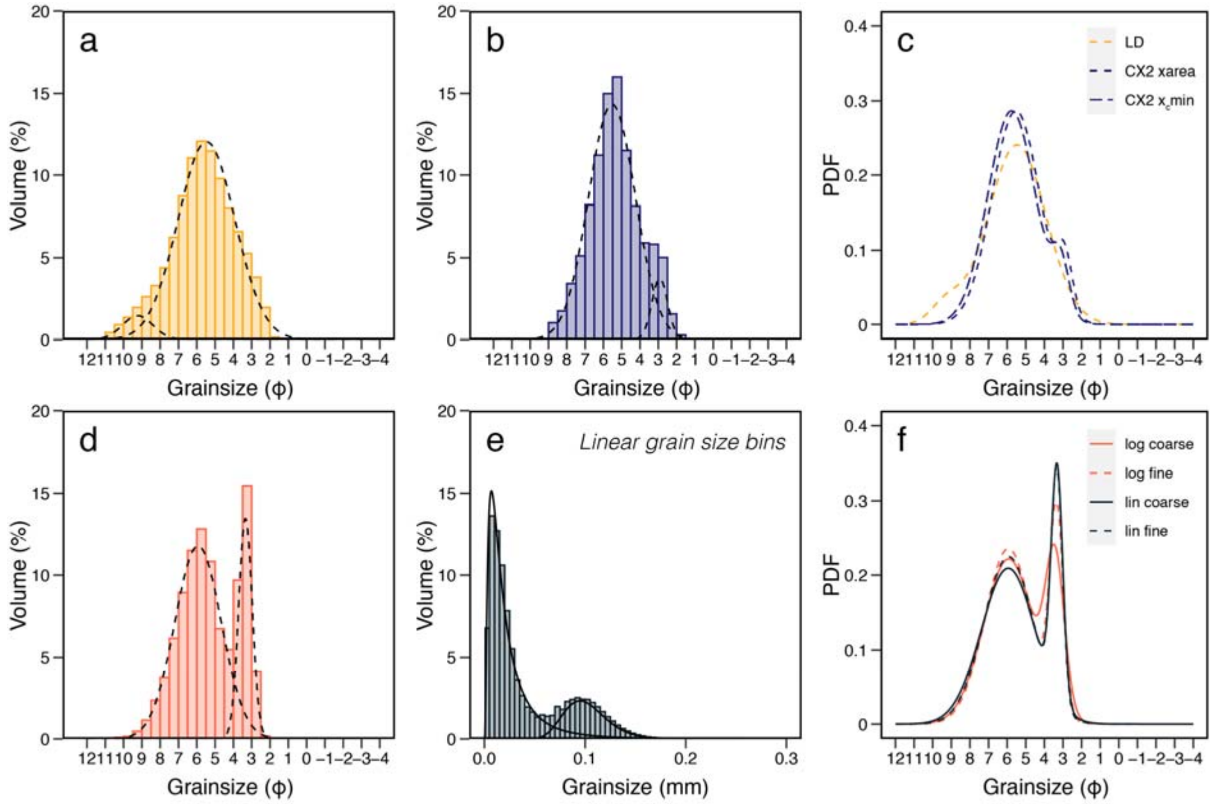

Figure 9 – Bimodal log-normal distributions fit to MSH GSDs. a) GSD of DAVIS11 measured with laser diffraction (Durant et al. 2009) fit with two log-normal subpopulations. b) GSD of MSH_RV measured by X-jet (xarea) fit with two log-normal subpopulations. c) Comparison between bimodal distributions according to method and CX2 size parameter. d) GSD of MSH_SB sample in half-φ bins with two log-normal subpopulations. e) GSD of MSH_SB sample binned on the linear scale (5 μm) fitted with two log-normal subpopulations. f) Comparison between distributions fit on the φ and linear scales, as well as coarse (full φ; 10 μm) and fine bins (half φ; 5 μm).

5. Discussion

The CX2 is a valuable tool for simultaneously analysing the size and shape of non-spherical particles, such as tephra, thanks to the dynamic image analysis (DIA) principle. Here we discuss some of the benefits of DIA relative to more widely used methods of grain size analysis (see section 2). We also consider the limitations of grain size analysis methods, in particular, for studying ultra-fine (<10 μm) particles. Finally, we discuss the implications of different grain size methods for using and interpreting grain size data for the purposes of studying explosive volcanism.

5.1. Appraisal of dynamic image analysis for measuring non-spherical particles

DIA facilitates rapid and simultaneous quantification of the size and shape of volcanic tephra whilst other particle analysis techniques compromise on either particle shape information or analysis time. For example, laser diffraction contains no shape information but is fast, whereas SEM image analysis provides excellent particle shape data but requires time consuming image processing as well as assumptions about particle size. Specifically, the CX2 has the added benefit of measuring multiple size descriptors (Figs. 2 - 4). Not only does this supplement shape parameterisation, but it can help explain some of the grain size anomalies described in the literature. For example, the large grains reported in cryptotephra studies (Stevenson et al. 2015; Saxby et al. 2019) are quantified according to their $x_{Fe}max$ size. Our data show that the $x_{Fe}max$ grain sizes within individual sieve classes can extend beyond the range predicted by the size aperture (Fig. 4). In other words, sieve data can mask extreme particle sizes if you assume the maximum particle size is equal to the passing sieve aperture. Furthermore, we have confirmed that sieving sorts by both particle size and shape and that the range of $x_{Fe}max$ within a sieve fraction can be extreme for elongated and flat particles such as the Campanian Ignimbrite tephra (Fig. 4g).

Collection of multiple size parameters makes CX2-derived GSDs compatible and comparable with a range of other widely used grain size measurement methods. The $x_c min$ parameter closely matches the expected sieve range (Fig. 4), meaning that there is limited data loss and manipulation required to combine coarse and fine-grained methods. Laser diffraction (LD) estimates xarea when using Mie theory and $x_{Fe}max$ when using the Fraunhofer approximation. Aside from differences of <10 μm, we find that CX2 and LD GSDs are comparable, which is advantageous for comparisons with established grain size datasets (e.g. Durant et al. 2009; Engwell et al. 2014; Liu et al. 2017).

An additional benefit of DIA is that it quantifies GSDs in terms of volume percent, such that coarse (>125 µm) GSDs measured using DIA are compatible with other volume-based methods of grain size analysis (laser diffraction, image analysis). This means there is no need to convert between volume and mass which requires an assumption of sample density. Furthermore, using DIA analysis in parallel with sieve analysis shows that mass-based GSDs can be influenced by dense grain size fractions that arise from crystal concentrations (Fig. 8). Whilst the relative density distributions calculated from the parallel sieve and CX2 analyses cannot be used quantitatively (Fig. 8d), this approach provides a fast way to qualitatively investigate changes in particle density and it clearly highlights the crystal concentration in the 2-3 φ size range and can be used to identify size classes that require direct density measurements, which are more accurate but time consuming.

Although DIA has clear advantages for characterising tephra it also has limitations. Firstly, the minimum grain size measured by the CX2 is 0.8 µm, which is coarser than laser diffraction techniques (e.g. the Mastersizer 3000 minimum size is 0.01 µm). Sub-micron and nano scale particles are important for understanding satellite retrievals of volcanic ash in the atmosphere (e.g. Prata 1989; Muñoz et al. 2004; Prata and Prata 2012; Miffre et al. 2012), the health impacts of volcanic ash (Horwell and Baxter 2006; Horwell 2007), the electrification of volcanic plumes (e.g. James et al. 2000; Miura et al. 2002; Cimarelli et al. 2014) and the meteorological (Durant et al. 2008; Gibbs et al. 2015) and climactic effects of volcanic eruptions (Rampino and Self 1993; Dartevelle et al. 2002). As the proportion of particles <0.8 µm cannot be determined with the CX2, characterisation of the ultra-fine GSD is incomplete.

The minimum grain size and image resolution limits of the CX2 also have consequences for the shape measurements. As the DIA approaches the limit of image resolution, the edge detection for particles will be increasingly affected by image pixilation. This could lead to over smoothed or imprecise particle perimeters, which will be particularly significant for shape parameters that include particle perimeter (e.g. SPHT; Fig. 5; Liu et al. 2015). Additionally, the shape parameter formulae are not always consistent with other studies, for example, the convexity formulation used by the CX2 software is the equivalent of the 'solidity' parameter used by Cioni et al. (2014) and Liu et al. (2015). The CX2 is also limited to 2D shape characterisation whereas some studies of volcanic ash compute 3D shape parameters (e.g. sphericity; Ganser 1993; Dioguardi et al. 2017; Saxby et al. 2018). Whilst it is common that shape parameters have different definitions and formulations, it is not possible to modify the shape parameter formulations in the CX2 software, meaning that not all shape parameters and formulations can be computed and compared with other shape studies (e.g. Riley et al. 2003; Liu et al. 2015; Leibrandt and Le Pennec 2015).

5.2. Significance of comprehensive grain size characterisation

DIA is a valuable method for scrutinising the size and shape of distal ash samples simultaneously. The median grain size of distal ash deposits is known to stabilise at large distances from source (Fig.10; Engwell et al. 2014; Engwell and Eychenne 2016; Cashman and Rust 2020). The transition to the stable distal grain size occurs when the sedimentation of particles is no longer governed by Stokes law (Engwell and Eychenne 2016). However, analysis of distal MSH, Mazama and Campanian Ignimbrite ash shows that the median grain size of distal ash is not uniform across different eruptions meaning particle ‘size’ alone cannot explain this phenomenon (Fig. 10). We propose that differences in how particle size is quantified can partly explain the dissimilar distal grain sizes. For example, the laser diffraction method used to measure the GSD of the Campanian Ignimbrite tephra (Fraunhofer theory; Engwell et al. 2014) produces the equivalent of an $x_{Fe}max$ distribution (particle long axis), which may explain the apparent coarse distal grain size when compared to GSDs quantified as $x_{c}min$ (sieving) or xarea (laser diffraction using Mie theory).

Another disparity in how size is quantified exists between the inputs used by ash dispersion models and how we measure physical ash samples. Particle size distributions (PSDs) used by ash dispersion models are specified in terms of equivalent volume sphere diameter (D_v; Beckett et al. 2015; Saxby et al. 2018). Saxby et al. (2020) used 3D data of ash volumes to demonstrate the divergence between volume-equivalent sphere diameters and long axis ($x_{Fe}max$) measurements that result from extreme ash morphologies (Fig. 11). If we assume an average shard thickness of ~10 µm, the difference between the maximum length (L or x_{Fe}max) and equivalent sphere diameter of a Campanian Ignimbrite ash shard (D_V) is more than 5-fold (Fig. 11). Similarly, to quantify particle size as an equivalent volume sphere diameter, 2D image analysis techniques assume that the equivalent area circle diameter (xarea) can be converted directly to D_V, although the relation between xarea and D_V varies with the 3D shape.

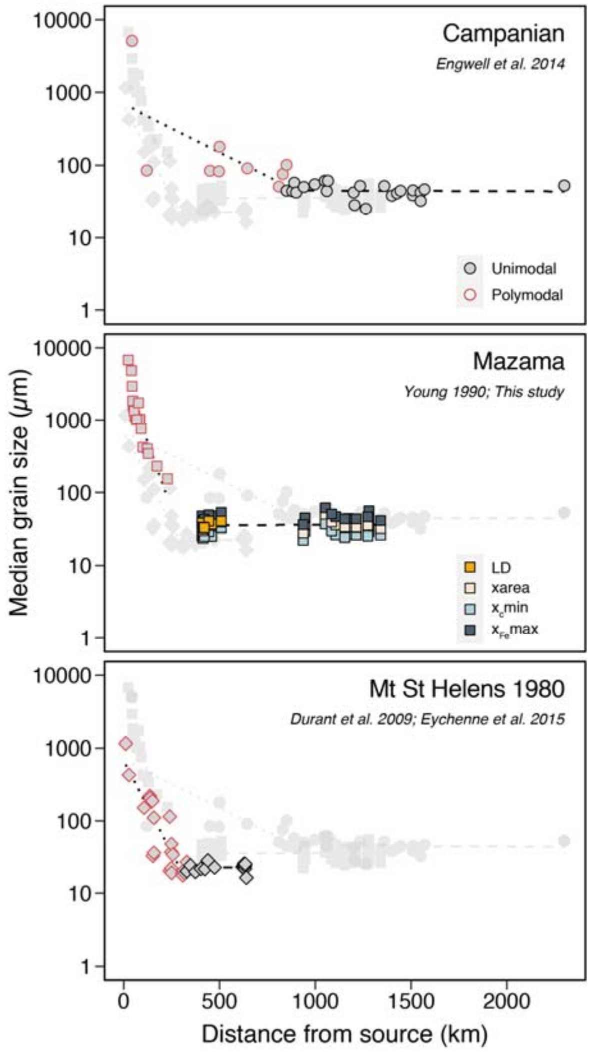

Figure 10 – Grain size of distal tephras with distance from source. a) Campanian tephra with grain size distributions and sub-populations from Engwell et al. (2014). b) Mazama tephra with data from Young (1990), Buckland et al. 2020 and this study. c) Mount St Helens 1980 data from Durant et al. (2009) and deconvolution by Engwell et al. (2015).

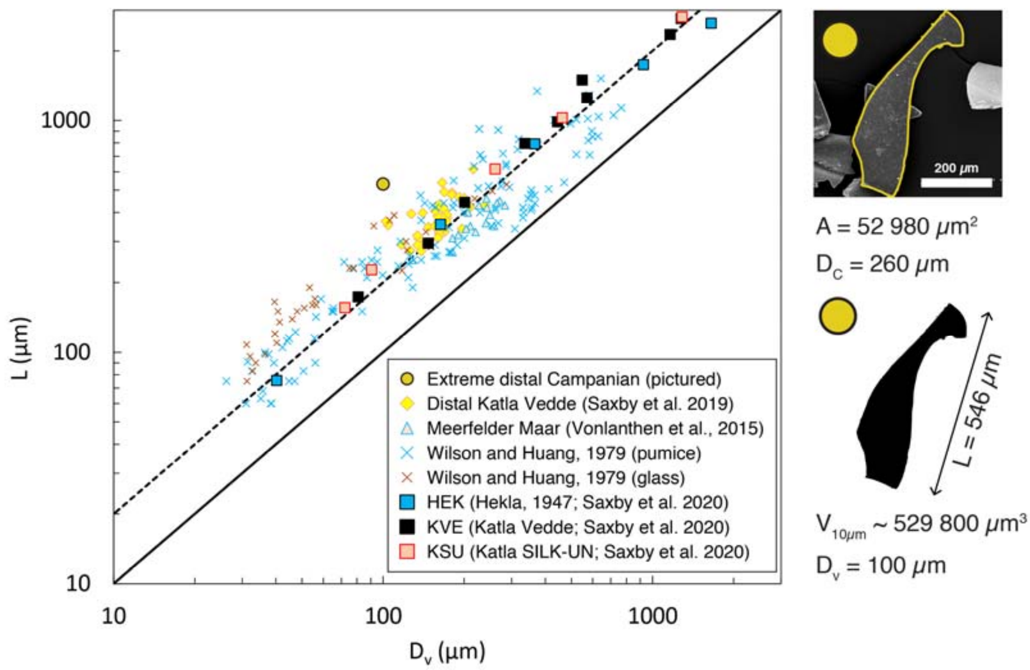

Figure 11 – Volume-equivalent sphere diameter D_v vs long axis length L with example extreme Campanian Ignimbrite ash shard (circle symbol). A is the 2D area of the particle and D_c is the equivalent circle diameter. Square symbols show means (from X-ray CT data, Saxby et al. 2020); diamond symbols are from optical measurements (Saxby et al. 2019) and all other symbols are individual particle measurements collated in Saxby et al. (2020). Solid line: y=x, dashed line: y=2x. The SE image (top right) and binary image (bottom right) illustrate how the long axis (L) and equivalent circle diameter (Dc) is determined from 2D image analysis.

Another explanation for the coarse grain size of the distal Campanian Ignimbrite and Mazama samples relative to the MSH distal tephra is related to the influence of particle shape (Fig. 12). Non-spherical particles have higher drag coefficients and lower settling velocities than volume-equivalent spherical particles (Mele et al. 2011; Dioguardi et al. 2017; Saxby et al. 2018, 2019). The distal Campanian Ignimbrite ash has the lowest range of SPHT distributions reflecting the high proportion of glass shards and plates (Fig. 12b). The MSH 1980 tephra on the other hand, has higher overall SPHT and the particles appear closer to ellipses (Fig. 12d). Therefore, it is likely that the differences in the medial distal grain sizes (Fig. 11) are a result of the combination in different parameterisations of size and the impact of particle shape on terminal settling velocities. It is also possible that the differences in distal median grain size (Fig. 10) are real and reflect the initial fragmentation processes. For instance, the fine-grained MSH ash (Md ~20 µm) has been attributed to the co-PDC plume formed as a result of the lateral blast (Eychenne et al. 2015).

Particle density also governs the settling velocity of tephra. Parallel sieve and CX2 analyses, paired with density measurements, highlight the non-uniform density distribution in coarse Mazama tephras (Fig. 8); parallel analyses provided a qualitative assessment of density across the size array. The density distribution measured for the coarse Mazama samples (Fig. 8c) differs from the sigmoidal distributions of clast density that have been measured and modelled in other tephra deposits (e.g. Barberi et al. 1989; Koyaguchi and Ohno 2001; Bonadonna and Phillips 2003; Eychenne and Le Pennec 2012). The main difference is that the maximum measured density (~2.6 gcm^{-3}) exceeds the glass density (~2.1 gcm^{-3}), which is often used to approximate the density of the very fine ash that is typically dominated by glass fragments. Whilst the high proportion of lithics and iron titanium oxides in the Mazama tephra contribute to this extreme density value, crystal concentrations are frequently observed in fallout deposits (Taupo, Walker 1981; MSH, Carey and Sigurdsson 1982; Santa Maria, Williams and Self 1983) and it is likely that their occurrence could influence interpretations of GSDs especially when quantified as mass distributions without reference to parallel componentry analyses. Moreover, componentry is often determined from SEM images (Liu et al. 2017; Buckland et al. 2018; McNamara et al. 2018); without consideration of particle density, the componentry proportions from SEM images do not map directly to the proportion of the sample mass. This has implications for methods that use the proportion of crystals in deposits to calculate erupted volumes (Walker 1980; Pyle 1989; Fierstein and Nathenson 1992; Scarpati et al. 2014). Whilst crystal and lithic concentrations pose a challenge for grain size analysis methods, sample density does converge on the glass density at small grain sizes (distal ash). Understanding where the transition to stable ash density occurs is important for ash dispersion modelling and likely relates to the eruption intensity and parent magma.

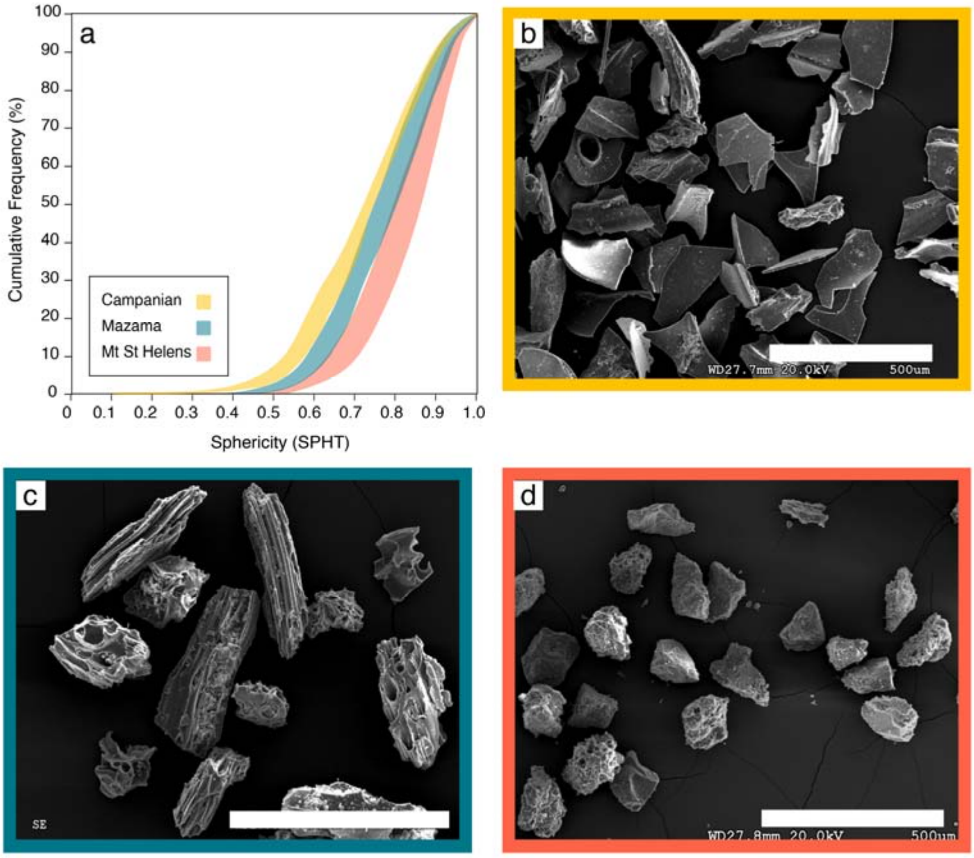

Figure 12 – Sphericity distributions and SE images of distal tephras. a) Ranges of multiple individual SPHT distributions for each distal tephra suite. b-d) Images collected on the Hitachi S-3500N SEM at the University of Bristol in secondary electron mode. Samples were sieved between 90-125 μm, mounted on carbon stubs gold coated. Images were collected at 20kV using a working distance of ~27.7 mm. White bars are 500 μm in all images.

6. Conclusions

Quantifying the size of an irregular shaped particle can be ambiguous and the range of methods available to analyse grain size adds another source of variability to the definition of particle 'size' (Bagheri et al. 2015). The heterogenous nature of tephra, which is often a mixture of components with varied particle densities and shapes, also complicates size analysis. We have shown, however, that dynamic image analysis methods can provide a useful protocol for characterising the size and shape of irregular particles. For example, we show that sieving (which in often considered to sort by size) sorts by size and shape and that for non-spherical particles, the size range of a sieve fraction depends on the size parameter used (Sanford and Swift 1971). In contrast, DIA can measure continuously over a large size range and GSDs can be quantified according to multiple size measures. DIA also quantified GSDs as volume distributions which the facilitates comparisons between DIA methods and other techniques such as laser diffraction. Using grain size statistics, we show that both GSDs and the interpretation of GSDs are sensitive to the method of particle size analysis. For example, different sub-populations may be deconvolved from multi-modal deposits that have been analysed in different ways. This suggests that caution should be used when comparing GSDs and their statistics for samples that have been analysed using different methods. Similarly, associating eruptive processes to grain size sub-populations could be influenced by the starting GSD and the method of deconvolution.

The discrepancy between volcanic ash dispersion models PSDs and ground-based GSDs are explained by a combination of different analysis methods, different size parameterisation, different size ranges and the impact of non-spherical particles. For instance, large distal ash grains often exhibit extreme shapes that when described using x_{Fe}max or their long axis appear oversized compared to their volume-equivalent sphere diameter (Saxby et al. 2020). Characterising the 3D morphology of volcanic particles is impractical on a large scale, which is why existing methods of grain size analysis are favoured. In parallel with quantitative shape data, we have shown that 2D methods of size analysis such as DIA can provide insight into the properties of distal ash. Careful consideration of size methods and the impact of non-spherical particles have in part explained the differences between the grain size of distal tephras. This information could be used to inform the PSDs used by ash dispersion models, especially if predicting long range ash dispersal is the main goal.

Appendix A – Grain size statistics and distribution fitting

A.1. Definitions of parameters and probability density functions

The Folk and Ward (FW; 1957) graphical statistics are calculated using interpolated values from the cumulative distribution function (Fig. A1b). The parameters are calculated using the formulas below:

$$\mu_{FW} = \frac{\varphi_{16} + \varphi_{50} + \varphi_{84}}{3} \qquad (A.1)$$

$$\sigma_{FW} = \frac{\varphi_{84} - \varphi_{16}}{4} + \frac{\varphi_{95} + \varphi_{5}}{6.6} \qquad (A.2)$$

$$Sk = \frac{\varphi_{16} + \varphi_{84} - 2\varphi_{50}}{2(\varphi_{84} - \varphi_{16})} + \frac{\varphi_{5} + \varphi_{95} - 2\varphi_{50}}{2(\varphi_{95} - \varphi_{5})} \qquad (A.3)$$

$$K = \frac{\varphi_{95} - \varphi_{5}}{2.44(\varphi_{75} - \varphi_{25})} \qquad (A.4)$$

where μ_{FW} denotes the Folk and Ward mean, σ_{FW} is the standard deviation or sorting, Sk is the skewness and K is Kurtosis. φ_y is the value in φ where y denotes the percentile of the cumulative distribution, e.g. φ_{50} is the median grain size (Fig. A1b). The values of sorting, skewness and Kurtosis then correspond to a qualitative classification according to the categories in Table A1.

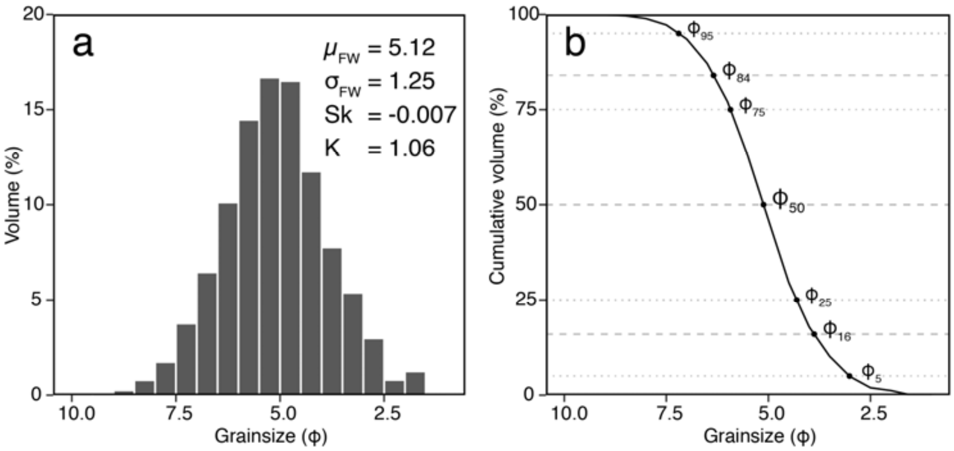

Figure A1 – Example of the FW parameters calculated for distal Mazama sample AP1. a) The grain size distribution measured using the CX2 quantified as the volume percent in each half-φ size fraction. b) Cumulative grain size distribution represented as the percentage coarser than the nominal grain size fraction with the interpolated values required for calculating the FW statistics plotted as black circles.

Table A1 – Descriptive terminology corresponding to the Folk and Ward parameters calculated for grain size data on the φ scale.

Sorting (σ_{FW})		Skewness (Sk)		Kurtosis (K)	
Very well sorted	<0.35	Very fine skewed	+0.3 to +1.0	Very platykurtic	<0.67
Well sorted	0.35 – 0.50	Fine skewed	+0.1 to +0.3	Platykurtic	0.67 – 0.90
Moderately well sorted	0.50 – 0.70	Symmetrical	+0.1 to -0.1	Mesokurtic	0.90 – 1.11
Moderately sorted	0.70 – 1.00	Coarse skewed	-0.1 to -0.3	Leptokurtic	1.11 – 1.50
Poorly sorted	1.00 – 2.00	Very coarse skewed	-0.3 to -1.0	Very leptokurtic	1.50 – 3.00
Very poorly sorted	2.00 – 4.00			Extremely leptokurtic	>3.00
Extremely poorly sorted	>4.00				

FW parameters assume that the GSD is log-normally distributed (normal on the φ-scale). However, GSDs can also be fit to probability density functions (PDFs) directly. When working with grain size data on the φ scale the GSD can be fit using a normal distribution which has the PDF:

$$f_{norm}(\varphi) = \frac{1}{\sigma_{\varphi}\sqrt{2\pi}} \exp\left[-\frac{1}{2}\left(\frac{\varphi - \mu_{\varphi}}{\sigma_{\varphi}}\right)^2\right] \quad (A.5)$$

where φ is the grain size in φ units, μ_{φ} denotes the mean and σ_{φ} is the standard deviation. This can be extended to facilitate the fitting of mixture models where the PDF is described as the sum of multiple normal distributions multiplied by their mixing proportion. For example, the PDF for a bimodal distribution which is the sum of two normal distributions is:

$$f_{bi-norm}(\varphi) = p_1 \frac{1}{\sigma_{\varphi 1}\sqrt{2\pi}} \exp\left[-\frac{1}{2}\left(\frac{\varphi - \mu_{\varphi 1}}{\sigma_{\varphi 1}}\right)^2\right] + p_2 \frac{1}{\sigma_{\varphi 2}\sqrt{2\pi}} \exp\left[-\frac{1}{2}\left(\frac{\varphi - \mu_{\varphi 2}}{\sigma_{\varphi 2}}\right)^2\right] \quad (A.6)$$

where p_1 and p_2 are the mixing proportions of each population. When fitting a normal distribution to GSDs on the φ-scale, it must be remembered that the mean and standard deviation relate to the logarithm of the data and that the GSD is log-normal in linear space. This is an important distinction because when data follows a log-normal distribution the mean, mode and median are not equal. Furthermore, data visualisation of GSDs on the φ-scale can be distorted (Fig. A1a).

It can be preferrable to fit log-normal PDFs directly to grain size data and to work in metric units as is standard procedure in engineering and aerosol science (Dartevelle et al. 2002). To fit a log-normal function, the grain size data cannot be on the φ-scale because d must be greater than 0 (Eq. A7). Therefore, the GSD must either be output using a linear bin configuration or exponentiated from the φ scale ($d = 2^{-\varphi}$). The PDF of a log-normal distribution is:

$$f_{lnorm}(d) = \frac{1}{d\sigma' \sqrt{2\pi}} \exp\left[-\frac{(\ln(d) - \mu')^2}{2\sigma'^2}\right] for\ d > 0 \qquad (A.7)$$

where d is the grain size in mm, μ' denotes the mean of the natural logarithm of the data and σ' is the standard deviation of the natural logarithm of the data. Using these parameters, the mean (μ), median (Md) and mode (Mo) can also then be calculated:

$$\mu_L = \exp\left[\mu' + \frac{1}{2}\sigma'^2\right] \qquad (A.8)$$

$$Md_L = \exp[\mu'] \qquad (A.9)$$

$$Mo_L = \exp[\mu' - \sigma'^2] \qquad (A.10)$$

where the μ_L is the mean, Md_L is the median and Mo_L is the mode of the log-normal distribution in mm units. Mixture models of log-normal distributions can also be used to describe GSDs where the PDF is the sum of the PDF of each sub-population multiplied by the mixing proportion:

$$f_{bi-lnorm}(d) = p_1 \frac{1}{d\sigma_1'\sqrt{2\pi}} \exp\left[-\left(\frac{\ln(d) - \mu_1'}{2\sigma_1'^2}\right)^2\right]$$

$$+ \ p_2 \frac{1}{d\sigma_2'\sqrt{2\pi}} \exp\left[-\left(\frac{\ln(d) - \mu_2'}{2\sigma_2'^2}\right)^2\right] \qquad (A.11)$$

Grain size distributions can also be described using a Weibull distribution which has the PDF:

$$f_{Weibull}(d) = \frac{k}{\lambda}\left(\frac{d}{\lambda}\right)^{k-1} \exp\left[-\left(\frac{d}{\lambda}\right)^k\right] for\ d \geq 0 \qquad (A.12)$$

where d is particle diameter in mm, k is the shape parameter and λ is the scale parameter. Similar to the log-normal distribution, the Weibull distribution cannot be fit to grain size data on the φ-scale so the GSD must be quantified in mm. GSDs can also be fit with mixtures of Weibull PDF, for example the PDF of a bimodal Weibull distribution is:

$$f_{bi-Weibull}(d) = p_1 \frac{k_1}{\lambda_1}\left(\frac{d}{\lambda_1}\right)^{k_1-1} \exp\left[-\left(\frac{d}{\lambda_1}\right)^{k_1}\right] + p_2 \frac{k_2}{\lambda_2}\left(\frac{d}{\lambda_2}\right)^{k_2-1} \exp\left[-\left(\frac{d}{\lambda_2}\right)^{k_2}\right] \quad (A.13)$$

where p_1 and p_2 are the mixing proportions, k_1 and k_2 are the scale parameters, and λ_1 and λ_2 are the scale parameters.

The mean, median and mode of the Weibull distribution can be calculated from the shape and scale parameters using the equations:

$$\mu_W = \lambda \cdot \Gamma\left(\frac{1}{k} + 1\right) \quad (A.14)$$

$$Md_W = \lambda(ln\ 2)^{\frac{1}{k}} \quad (A.15)$$

$$Mo_W = \lambda\left(1 - \frac{1}{k}\right)^{\frac{1}{k}} \quad (A.16)$$

where the μ_W is the mean, Γ is the gamma function, Md_W is the median and Mo_W is the mode in mm units.

A.2. Methods of fitting distributions

GSDs are reported as histograms, in other words, the individual particle sizes are not known the proportion of the total mass or volume of particles is known within a grain size range. This is why graphical parameters and the method of moments have been favoured (Folk and Ward 1957; Blott and Pye 2001) as they can be easily calculated from binned data. An alternative approach is to find the best fit parameters of a chosen function (e.g. log-normal or Weibull) using least squares regression, typically by fitting the cumulative density function (e.g. Macías-García et al. 2004). Another method is to simulate measurements of individual particle sizes based on the proportion within each grain size bin, which facilitates the use of maximum likelihood estimation methods.

For this contribution we have used the latter approach of simulating data based on the measured GSD. We chose this approach because we found that the least squares regression approach was more sensitive to the grain size bin configuration than maximum likelihood estimates. We simulate the grain size data by assuming that the weight or volume percent within each grain size bin is equivalent to the number or frequency of measurements (n). We then generate a uniform distribution of grain size measurements, where the number of measurements is equal to m and the absolute value ranges between the minimum and maximum size of the bin. This simulated dataset can then be used to fit a range of PDFs.

We fit log-normal and Weibull distributions to the simulated data using the ‘fitdistrplus’ package in R (Delignette-Muller and Dutang 2015). An example of a normal, log-normal and Weibull distribution fit to a unimodal grain size distribution (distal Mazama) is shown in Figure A2. We fit bimodal distributions using the ‘mixfit’ function from the ‘mixR’ R package with example fits shown in Figure A3 (distal MSH).

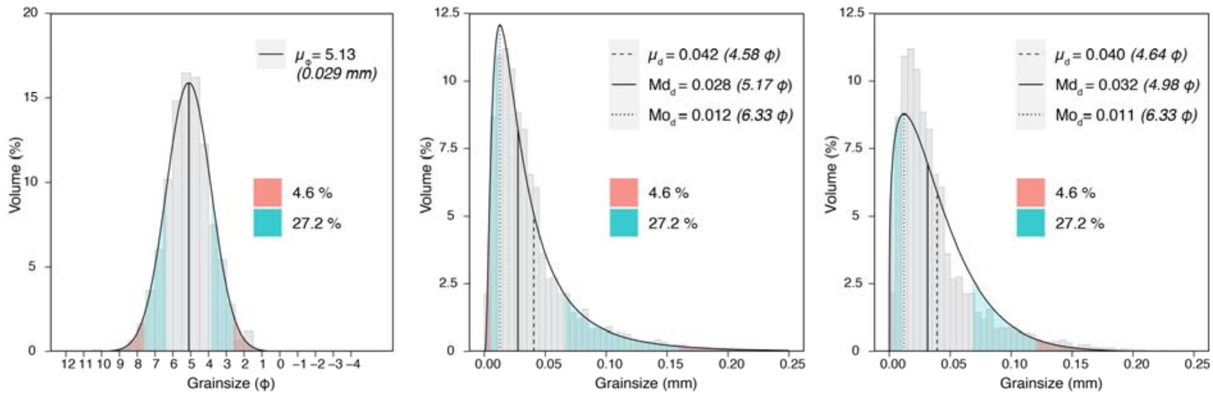

Figure A2 – Simulated grain size data for distal Mazama sample AP1 fit with a) normal; b) log-normal and c) Weibull probability density functions. The coloured segments correspond to >1 standard deviation, so the blue shaded area contains 27.2% of the distribution (±1 to 2σ) and the red shaded area contains 4.6% of the distribution (>2σ).

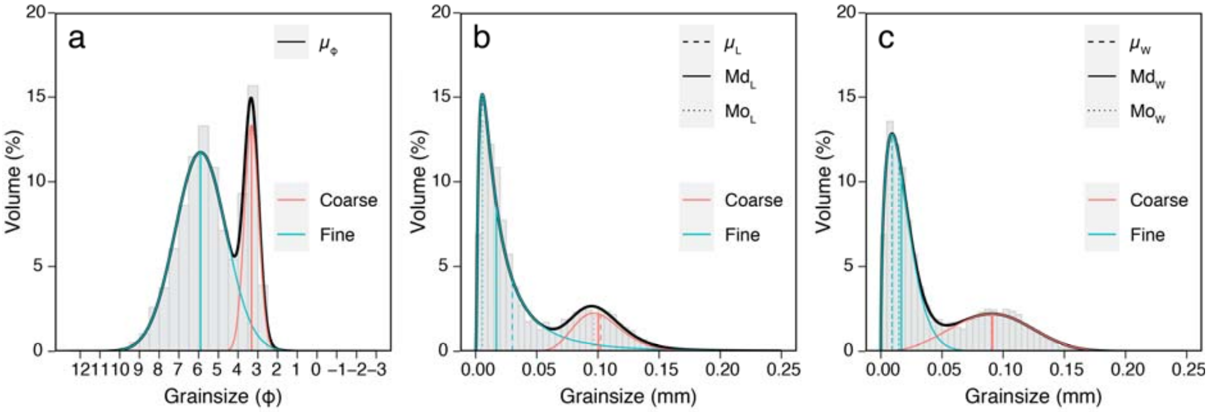

Figure A3 – Simulated grain size data for distal Mount St Helens sample SB fit with bimodal a) normal; b) log-normal and c) Weibull probability density functions. The coarse and fine sub-populations are indicated by the coloured PDFs with the mode, mean and median of each population also indicated by corresponding lines. The solid black line is the bimodal distribution according to Eqs. A6, 11 and 13

In the main text, we report the FW parameters and the parameters of bimodal normal distributions fit to data on the φ-scale (Eq. A6) to allow comparisons with previously published grain size statistics. This also avoids any confusion that might arise from comparing Weibull parameters determined by different fitting methods (e.g. DECOLOG; Eychenne et al. 2015).

References

Adachi A, Kobayashi T, Yamauchi H, Onogi S (2013) Detection of potentially hazardous convective clouds with a dual-polarized C-band radar. Atmospheric Measurement Techniques Discussions 6:

Alfano F, Bonadonna C, Watt S, et al (2016) Reconstruction of total grain size distribution of the climactic phase of a long-lasting eruption: the example of the 2008–2013 Chaitén eruption. Bull Volcanol 78:46. https://doi.org/10.1007/s00445-016-1040-5

Bagheri GH, Bonadonna C, Manzella I, Vonlanthen P (2015) On the characterization of size and shape of irregular particles. Powder Technology 270:141–153. https://doi.org/10.1016/j.powtec.2014.10.015

Barberi F, Cioni R, Rosi M, et al (1989) Magmatic and phreatomagmatic phases in explosive eruptions of Vesuvius as deduced by grain-size and component analysis of the pyroclastic deposits. Journal of Volcanology and Geothermal Research 38:287–307. https://doi.org/10.1016/0377-0273(89)90044-9

Bebbington M, Cronin SJ, Chapman I, Turner MB (2008) Quantifying volcanic ash fall hazard to electricity infrastructure. Journal of Volcanology and Geothermal Research 177:1055–1062. https://doi.org/10.1016/j.jvolgeores.2008.07.023

Beckett FM, Witham CS, Hort MC, et al (2015) Sensitivity of dispersion model forecasts of volcanic ash clouds to the physical characteristics of the particles. Journal of Geophysical Research: Atmospheres 120:11,636-11,652. https://doi.org/10.1002/2015JD023609

Beuselinck L, Govers G, Poesen J, et al (1998) Grain-size analysis by laser diffractometry: comparison with the sieve-pipette method. CATENA 32:193–208. https://doi.org/10.1016/S0341-8162(98)00051-4

Blake DM, Wilson TM, Cole JW, et al (2017) Impact of Volcanic Ash on Road and Airfield Surface Skid Resistance. Sustainability 9:1389. https://doi.org/10.3390/su9081389

Blott SJ, Pye K (2001) GRADISTAT: a grain size distribution and statistics package for the analysis of unconsolidated sediments. Earth Surface Processes and Landforms 26:1237–1248. https://doi.org/10.1002/esp.261

Bonadonna C, Cioni R, Pistolesi M, et al (2013) Determination of the largest clast sizes of tephra deposits for the characterization of explosive eruptions: a study of the IAVCEI commission on tephra hazard modelling. Bull Volcanol 75:680. https://doi.org/10.1007/s00445-012-0680-3

Bonadonna C, Folch A, Loughlin S, Puempel H (2012) Future developments in modelling and monitoring of volcanic ash clouds: outcomes from the first IAVCEI-WMO workshop on Ash Dispersal Forecast and Civil Aviation. Bulletin of volcanology 74:1–10

Bonadonna C, Genco R, Gouhier M, et al (2011) Tephra sedimentation during the 2010 Eyjafjallajökull eruption (Iceland) from deposit, radar, and satellite observations. Journal of Geophysical Research: Solid Earth 116:. https://doi.org/10.1029/2011JB008462

Bonadonna C, Houghton BF (2005) Total grain-size distribution and volume of tephra-fall deposits. Bulletin of Volcanology 67:441–456. https://doi.org/10.1007/s00445-004-0386-2

Bonadonna C, Phillips JC (2003) Sedimentation from strong volcanic plumes. Journal of Geophysical Research: Solid Earth 108:. https://doi.org/10.1029/2002JB002034

Brand BD, Bendaña S, Self S, Pollock N (2016) Topographic controls on pyroclastic density current dynamics: Insight from 18 May 1980 deposits at Mount St. Helens, Washington (USA). Journal of Volcanology and Geothermal Research 321:1–17. https://doi.org/10.1016/j.jvolgeores.2016.04.018

Brown RJ, Bonadonna C, Durant AJ (2012) A review of volcanic ash aggregation. Physics and Chemistry of the Earth, Parts A/B/C 45:65–78

Brown WK, Wohletz KH (1995) Derivation of the Weibull distribution based on physical principles and its connection to the Rosin–Rammler and lognormal distributions. Journal of Applied Physics 78:2758–2763. https://doi.org/10.1063/1.360073

Buckland HM, Cashman KV, Engwell SL, Rust AC (2020) Sources of uncertainty in the Mazama isopachs and the implications for interpreting distal tephra deposits from large magnitude eruptions. Bull Volcanol 82:23. https://doi.org/10.1007/s00445-020-1362-1

Buckland HM, Eychenne J, Rust AC, Cashman KV (2018) Relating the physical properties of volcanic rocks to the characteristics of ash generated by experimental abrasion. Journal of Volcanology and Geothermal Research 349:335–350. https://doi.org/10.1016/j.jvolgeores.2017.11.017

Burden RE, Phillips JC, Hincks TK (2011) Estimating volcanic plume heights from depositional clast size. Journal of Geophysical Research: Solid Earth 116:. https://doi.org/10.1029/2011JB008548

Capaccioni B, Valentini L, Rocchi MBL, et al (1997) Image analysis and circular statistics for shape-fabric analysis: applications to lithified ignimbrites. Bull Volcanol 58:501–514. https://doi.org/10.1007/s004450050158

Carey S, Sparks R (1986) Quantitative models of the fallout and dispersal of tephra from volcanic eruption columns. Bulletin of Volcanology 48:109–125

Carey SN, Sigurdsson H (1982) Influence of particle aggregation on deposition of distal tephra from the MAy 18, 1980, eruption of Mount St. Helens volcano. Journal of Geophysical Research: Solid Earth 87:7061–7072. https://doi.org/10.1029/JB087iB08p07061

Carey SN, Sigurdsson H, Sparks RSJ (1988) Experimental studies of particle-laden plumes. Journal of Geophysical Research: Solid Earth 93:15314–15328. https://doi.org/10.1029/JB093iB12p15314

Casadevall TJ (1994) The 1989–1990 eruption of Redoubt Volcano, Alaska: impacts on aircraft operations. Journal of Volcanology and Geothermal Research 62:301–316. https://doi.org/10.1016/0377-0273(94)90038-8

Cashman KV, Rust AC (2020) Far-travelled ash in past and future eruptions: combining tephrochronology with volcanic studies. Journal of Quaternary Science 35:11–22. https://doi.org/10.1002/jqs.3159

Castro MDL, Andronico D (2008) Operazioni di base per la misura della distribuzione granulometrica di particelle vulcaniche tramite il CAMSIZER. Instituto Nazionale di Geofisica e Vulcanologia, Catania

Cimarelli C, Alatorre-Ibargüengoitia MA, Kueppers U, et al (2014) Experimental generation of volcanic lightning. Geology 42:79–82. https://doi.org/10.1130/G34802.1

Cioni R, Pistolesi M, Bertagnini A, et al (2014) Insights into the dynamics and evolution of the 2010 Eyjafjallajökull summit eruption (Iceland) provided by volcanic ash textures. Earth and Planetary Science Letters 394:111–123. https://doi.org/10.1016/j.epsl.2014.02.051

Coltelli M, Miraglia L, Scollo S (2008) Characterization of shape and terminal velocity of tephra particles erupted during the 2002 eruption of Etna volcano, Italy. Bull Volcanol 70:1103–1112. https://doi.org/10.1007/s00445-007-0192-8

Cooper CL, Savov IP, Swindles GT (2019) Standard chemical-based tephra extraction methods significantly alter the geochemistry of volcanic glass shards. Journal of Quaternary Science 34:697–707. https://doi.org/10.1002/jqs.3169

Costa A, Pioli L, Bonadonna C (2016) Assessing tephra total grain-size distribution: Insights from field data analysis. Earth and Planetary Science Letters 443:90–107. https://doi.org/10.1016/j.epsl.2016.02.040

Cox L, Wood J, Fan J, Huang Y (2017) Experimental Separation of Non-spherical Ash Particles by Terminal Velocity. University of Bristol

Cyr M, Tagnit-Hamou A (2001) Particle size distribution of fine powders by LASER diffraction spectrometry. Case of cementitious materials. Mat Struct 34:342–350. https://doi.org/10.1007/BF02486485

Dartevelle S, Ernst GGJ, Stix J, Bernard A (2002) Origin of the Mount Pinatubo climactic eruption cloud: Implications for volcanic hazards and atmospheric impacts. Geology 30:663–666. https://doi.org/10.1130/0091-7613(2002)030<0663:OOTMPC>2.0.CO;2

Delignette-Muller ML, Dutang C (2015) fitdistrplus: An R Package for Fitting Distributions. Journal of Statistical Software 64:1–34

Dioguardi F, Mele D, Dellino P, Dürig T (2017) The terminal velocity of volcanic particles with shape obtained from 3D X-ray microtomography. Journal of Volcanology and Geothermal Research 329:41–53. https://doi.org/10.1016/j.jvolgeores.2016.11.013

Dugmore AJ, Newton AJ (1992) Thin tephra layers in peat revealed by X-radiography. Journal of Archaeological Science 19:163–170. https://doi.org/10.1016/0305-4403(92)90047-7

Durant AJ, Rose WI, Sarna-Wojcicki AM, et al (2009) Hydrometeor-enhanced tephra sedimentation: Constraints from the 18 May 1980 eruption of Mount St. Helens. Journal of Geophysical Research: Solid Earth 114:. https://doi.org/10.1029/2008JB005756

Durant AJ, Shaw RA, Rose WI, et al (2008) Ice nucleation and overseeding of ice in volcanic clouds. Journal of Geophysical Research: Atmospheres 113:. https://doi.org/10.1029/2007JD009064

Dürig T, White JDL, Zimanowski B, et al (2020) Deep-sea fragmentation style of Havre revealed by dendrogrammatic analyses of particle morphometry. Bull Volcanol 82:67. https://doi.org/10.1007/s00445-020-01408-1

Engwell SL, Eychenne J (2016) Contribution of fine ash to the atmosphere from plumes associated with pyroclastic density currents. In: Volcanic Ash: Hazard Observation. Elsevier, pp 67–85

Engwell SL, Sparks RSJ, Carey S (2014) Physical characteristics of tephra layers in the deep sea realm: the Campanian Ignimbrite eruption. Geological Society, London, Special Publications 398:47–64. https://doi.org/10.1144/SP398.7

Eychenne J, Cashman K, Rust A, Durant A (2015) Impact of the lateral blast on the spatial pattern and grain size characteristics of the 18 May 1980 Mount St. Helens fallout deposit. Journal of Geophysical Research: Solid Earth 120:6018–6038. https://doi.org/10.1002/2015JB012116

Eychenne J, Le Pennec J-L (2012) Sigmoidal particle density distribution in a subplinian scoria fall deposit. Bull Volcanol 74:2243–2249. https://doi.org/10.1007/s00445-012-0671-4

Eychenne J, Le Pennec J-L, Troncoso L, et al (2012) Causes and consequences of bimodal grain-size distribution of tephra fall deposited during the August 2006 Tungurahua eruption (Ecuador). Bull Volcanol 74:187–205. https://doi.org/10.1007/s00445-011-0517-5

Fairbridge RW, Bourgeois Joanne (1978) The Encyclopedia of sedimentology. Dowden, Hutchinson & Ross ;, Stroudsburg, Pa.

Fenner CN (1937) Tuffs and other volcanic deposits of Katmai and Yellowstone Park. Eos, Transactions American Geophysical Union 18:236–239. https://doi.org/10.1029/TR018i001p00236

Fierstein J, Nathenson M (1992) Another look at the calculation of fallout tephra volumes. Bulletin of Volcanology 54:156–167. https://doi.org/10.1007/BF00278005

Figueiredo MM (2006) Electrozone Sensing in Particle Size Analysis. In: Encyclopedia of Analytical Chemistry. American Cancer Society

Fisher RV (1964) Maximum size, median diameter, and sorting of tephra. Journal of Geophysical Research (1896-1977) 69:341–355. https://doi.org/10.1029/JZ069i002p00341

Folk RL, Ward WC (1957) Brazos River bar [Texas]; a study in the significance of grain size parameters. Journal of Sedimentary Research 27:3–26. https://doi.org/10.1306/74D70646-2B21-11D7-8648000102C1865D

Freret-Lorgeril V, Donnadieu F, Eychenne J, et al (2019) In situ terminal settling velocity measurements at Stromboli volcano: Input from physical characterization of ash. Journal of Volcanology and Geothermal Research 374:62–79. https://doi.org/10.1016/j.jvolgeores.2019.02.005

Ganser GH (1993) A rational approach to drag prediction of spherical and nonspherical particles. Powder Technology 77:143–152

Genareau K, Wallace KL, Gharghabi P, Gafford J (2019) Lightning Effects on the Grain Size Distribution of Volcanic Ash. Geophysical Research Letters 46:3133–3141. https://doi.org/10.1029/2018GL081298

Gibbs A, Charman M, Schwarzacher W, Rust AC (2015) Immersion freezing of supercooled water drops containing glassy volcanic ash particles. GeoResJ 7:66–69. https://doi.org/10.1016/j.grj.2015.06.002

Gibbs RJ, Matthews MD, Link DA (1971) The relationship between sphere size and settling velocity. Journal of Sedimentary Research 41:7–18. https://doi.org/10.1306/74D721D0-2B21-11D7-8648000102C1865D

Gouhier M, Eychenne J, Azzaoui N, et al (2019) Low efficiency of large volcanic eruptions in transporting very fine ash into the atmosphere. Scientific Reports 9:1–12. https://doi.org/10.1038/s41598-019-38595-7

Hadley D, Hufford GL, Simpson JJ (2004) Resuspension of relic volcanic ash and dust from Katmai: still an aviation hazard. Weather and forecasting 19:829–840. https://doi.org/10.1175/1520-0434(2004)019<0829:RORVAA>2.0.CO;2

Hails JR, Thompson BS, Cummings L (1973) An Appraisal of the Significance of Sieve Intervals in Grain Size Analysis for Environmental Interpretation. Journal of Sedimentary Research 43:

Heiken G (1972) Morphology and Petrography of Volcanic Ashes. GSA Bulletin 83:1961–1988. https://doi.org/10.1130/0016-7606(1972)83[1961:MAPOVA]2.0.CO;2

Hobbs PV, Radke LF, Lyons JH, et al (1991) Airborne measurements of particle and gas emissions from the 1990 volcanic eruptions of Mount Redoubt. Journal of Geophysical Research: Atmospheres 96:18735–18752. https://doi.org/10.1029/91JD01635

Horwell C (2007) Grain-size analysis of volcanic ash for the rapid assessment of respiratory health hazard. Journal of Environmental Monitoring 9:1107–1115. https://doi.org/10.1039/B710583P

Horwell CJ, Baxter PJ (2006) The respiratory health hazards of volcanic ash: a review for volcanic risk mitigation. Bull Volcanol 69:1–24. https://doi.org/10.1007/s00445-006-0052-y

Horwell CJ, Sparks RSJ, Brewer TS, et al (2003) Characterization of respirable volcanic ash from the Soufrière Hills volcano, Montserrat, with implications for human health hazards. Bull Volcanol 65:346–362. https://doi.org/10.1007/s00445-002-0266-6

Inman DL (1952) Measures for describing the size distribution of sediments. Journal of Sedimentary Research 22:125–145. https://doi.org/10.1306/D42694DB-2B26-11D7-8648000102C1865D

James MR, Lane SJ, Gilbert JS (2000) Volcanic plume electrification: Experimental investigation of a fracture-charging mechanism. Journal of Geophysical Research: Solid Earth 105:16641–16649. https://doi.org/10.1029/2000JB900068

Johnson B, Turnbull K, Brown P, et al (2012) In situ observations of volcanic ash clouds from the FAAM aircraft during the eruption of Eyjafjallajökull in 2010. Journal of Geophysical Research: Atmospheres 117:

Jones TJ, McNamara K, Eychenne J, et al (2016) Primary and secondary fragmentation of crystal-bearing intermediate magma. Journal of Volcanology and Geothermal Research 327:70–83. https://doi.org/10.1016/j.jvolgeores.2016.06.022

Jonkers L, Prins MA, Brummer G-JA, et al (2009) Experimental insights into laser diffraction particle sizing of fine-grained sediments for use in palaeoceanography. Sedimentology 56:2192–2206. https://doi.org/10.1111/j.1365-3091.2009.01076.x

Jutzeler M, Proussevitch AA, Allen SR (2012) Grain-size distribution of volcaniclastic rocks 1: A new technique based on functional stereology. Journal of Volcanology and Geothermal Research 239–240:1–11. https://doi.org/10.1016/j.jvolgeores.2012.05.013

Komar PD, Cui B (1984) The analysis of grain-size measurements by sieving and settling-tube techniques. Journal of Sedimentary Research 54:603–614. https://doi.org/10.1306/212F8481-2B24-11D7-8648000102C1865D

Koyaguchi T, Ohno M (2001) Reconstruction of eruption column dynamics on the basis of grain size of tephra fall deposits: 1. Methods. Journal of Geophysical Research: Solid Earth 106:6499–6512. https://doi.org/10.1029/2000JB900426

Kozono T, Iguchi M, Miwa T, et al (2019) Characteristics of tephra fall from eruptions at Sakurajima volcano, revealed by optical disdrometer measurements. Bull Volcanol 81:41. https://doi.org/10.1007/s00445-019-1300-2

Krumbein WC (1934) Size frequency distributions of sediments. Journal of Sedimentary Research 4:65–77. https://doi.org/10.1306/D4268EB9-2B26-11D7-8648000102C1865D

Kylling A, Kahnert M, Lindqvist H, Nousiainen T (2014) Volcanic ash infrared signature: porous non-spherical ash particle shapes compared to homogeneous spherical ash particles. Atmospheric Measurement Techniques 7:919–929. https://doi.org/10.5194/amt-7-919-2014

Lacroix A (1904) La Montagne Pelée et ses éruptions. Masson

Leadbetter S, Hort M, Löwis S, et al (2012) Modeling the resuspension of ash deposited during the eruption of Eyjafjallajökull in spring 2010. Journal of Geophysical Research: Atmospheres 117:

Leibrandt S, Le Pennec J-L (2015) Towards fast and routine analyses of volcanic ash morphometry for eruption surveillance applications. Journal of Volcanology and Geothermal Research 297:11–27. https://doi.org/10.1016/j.jvolgeores.2015.03.014

Liu EJ, Cashman KV, Beckett FM, et al (2014) Ash mists and brown snow: Remobilization of volcanic ash from recent Icelandic eruptions. Journal of Geophysical Research: Atmospheres 119:9463–9480. https://doi.org/10.1002/2014JD021598

Liu EJ, Cashman KV, Rust AC (2015) Optimising shape analysis to quantify volcanic ash morphology. GeoResJ 8:14–30

Liu EJ, Cashman KV, Rust AC, Höskuldsson A (2017) Contrasting mechanisms of magma fragmentation during coeval magmatic and hydromagmatic activity: the Hverfjall Fires fissure eruption, Iceland. Bull Volcanol 79:68. https://doi.org/10.1007/s00445-017-1150-8

Macías-García A, Cuerda-Correa EM, Díaz-Díez MA (2004) Application of the Rosin–Rammler and Gates–Gaudin–Schuhmann models to the particle size distribution analysis of agglomerated cork. Materials Characterization 52:159–164. https://doi.org/10.1016/j.matchar.2004.04.007

Malvern Panalytical (2020) Mastersizer 3000 | World’s Leading Particle Size Analyzer | Malvern Panalytical. In: Malvern Panalytical.

https://www.malvernpanalytical.com/en/products/product-range/mastersizer-range/mastersizer-3000. Accessed 27 Apr 2020

Mastin LG, Guffanti M, Servranckx R, et al (2009) A multidisciplinary effort to assign realistic source parameters to models of volcanic ash-cloud transport and dispersion during eruptions. Journal of Volcanology and Geothermal Research 186:10–21

McNamara K, Cashman KV, Rust AC, et al (2018) Using Lake Sediment Cores to Improve Records of Volcanism at Aluto Volcano in the Main Ethiopian Rift. Geochemistry, Geophysics, Geosystems 19:3164–3188. https://doi.org/10.1029/2018GC007686

Mele D, Costa A, Dellino P, et al (2020) Total grain size distribution of components of fallout deposits and implications for magma fragmentation mechanisms: examples from Campi Flegrei caldera (Italy). Bull Volcanol 82:31. https://doi.org/10.1007/s00445-020-1368-8

Mele D, Dellino P, Sulpizio R, Braia G (2011) A systematic investigation on the aerodynamics of ash particles. Journal of Volcanology and Geothermal Research 203:1–11. https://doi.org/10.1016/j.jvolgeores.2011.04.004

Meredith P (2019) Using the May 18, 1980 ash fallout deposit of Mount Saint Helens to compare methods of particle size analysis. Masters Thesis, University of Bristol

MicroTrac MRB (2020) CAMSIZER X2 - particle size & shape analyzer - Microtrac. In: MicroTrac MRB. https://www.microtrac.com/products/particle-size-shape-analysis/dynamic-image-analysis/camsizer-x2/function-features. Accessed 26 Mar 2020

Miffre A, David G, Thomas B, et al (2012) Volcanic aerosol optical properties and phase partitioning behavior after long-range advection characterized by UV-Lidar measurements. Atmospheric Environment 48:76–84. https://doi.org/10.1016/j.atmosenv.2011.03.057

Miura T, Koyaguchi T, Tanaka Y (2002) Measurements of electric charge distribution in volcanic plumes at Sakurajima Volcano, Japan. Bull Volcanol 64:75–93. https://doi.org/10.1007/s00445-001-0182-1

Miwa T, Iriyama Y, Nagai M, Nanayama F (2020) Sedimentation process of ashfall during a Vulcanian eruption as revealed by high-temporal-resolution grain size analysis and high-speed camera imaging. Progress in Earth and Planetary Science 7:3. https://doi.org/10.1186/s40645-019-0316-8

Moore BN (1934) Deposits of Possible Nuée Ardente Origin in the Crater Lake Region, Oregon. The Journal of Geology 42:358–375. https://doi.org/10.1086/624174

Mori T, Hashimoto T, Terada A, et al (2016) Volcanic plume measurements using a UAV for the 2014 Mt. Ontake eruption. Earth, Planets and Space 68:49. https://doi.org/10.1186/s40623-016-0418-0

Muñoz O, Volten H, Hovenier JW, et al (2004) Scattering matrices of volcanic ash particles of Mount St. Helens, Redoubt, and Mount Spurr Volcanoes. Journal of Geophysical Research: Atmospheres 109:. https://doi.org/10.1029/2004JD004684

OTT (2020) OTT Parsivel2 - Laser Weather Sensor. In: OTT Hydromet. https://www.ott.com/download/operating-instructions-present-weather-sensor-ott-parsivel2-without-screen-heating-1/. Accessed 3 Dec 2020

Palais JM, Germani MS, Zielinski GA (1992) Inter-hemispheric Transport of Volcanic Ash from a 1259 A.D. Volcanic Eruption to the Greenland and Antarctic Ice Sheets. Geophysical Research Letters 19:801–804. https://doi.org/10.1029/92GL00240

Panebianco JE, Mendez MJ, Buschiazzo DE, et al (2017) Dynamics of volcanic ash remobilisation by wind through the Patagonian steppe after the eruption of Cordón Caulle, 2011. Scientific Reports 7:45529. https://doi.org/10.1038/srep45529

Pavolonis MJ, Heidinger AK, Sieglaff J (2013) Automated retrievals of volcanic ash and dust cloud properties from upwelling infrared measurements. Journal of Geophysical Research: Atmospheres 118:1436–1458. https://doi.org/10.1002/jgrd.50173

Petäjä T, Laakso L, Grönholm T, et al (2012) In-situ observations of Eyjafjallajökull ash particles by hot-air balloon. Atmospheric Environment 48:104–112. https://doi.org/10.1016/j.atmosenv.2011.08.046

Pettijohn FJ (1949) Sedimentary rocks. Harper & Row New York

Pieri D, Ma C, Simpson JJ, et al (2002) Analyses of in-situ airborne volcanic ash from the February 2000 eruption of Hekla Volcano, Iceland. Geophysical Research Letters 29:19-1-19–4. https://doi.org/10.1029/2001GL013688

Pioli L, Bonadonna C, Pistolesi M (2019) Reliability of Total Grain-Size Distribution of Tephra Deposits. Sci Rep 9:10006. https://doi.org/10.1038/s41598-019-46125-8

Prata AJ (1989) Infrared radiative transfer calculations for volcanic ash clouds. Geophysical Research Letters 16:1293–1296. https://doi.org/10.1029/GL016i011p01293

Prata AJ, Grant IF (2001) Retrieval of microphysical and morphological properties of volcanic ash plumes from satellite data: Application to Mt Ruapehu, New Zealand. Quarterly Journal of the Royal Meteorological Society 127:2153–2179. https://doi.org/10.1002/qj.49712757615

Prata AJ, Prata AT (2012) Eyjafjallajökull volcanic ash concentrations determined using Spin Enhanced Visible and Infrared Imager measurements. Journal of Geophysical Research: Atmospheres 117:. https://doi.org/10.1029/2011JD016800

Pyle DM (1989) The thickness, volume and grainsize of tephra fall deposits. Bulletin of Volcanology 51:1–15

Rampino MR, Self S (1993) Climate-Volcanism Feedback and the Toba Eruption of ~74,000 Years Ago. Quaternary Research 40:269–280. https://doi.org/10.1006/qres.1993.1081

Riley CM, Rose WI, Bluth GJS (2003) Quantitative shape measurements of distal volcanic ash. Journal of Geophysical Research: Solid Earth 108:. https://doi.org/10.1029/2001JB000818

Roller PS (1931) Separation and Size Distribution of Microscopic Particles: An Air Analyzer for Fine Powders. U.S. Government Printing Office

Román-Sierra J, Muñoz-perez J j, Navarro-Pons M (2013) Influence of sieving time on the efficiency and accuracy of grain-size analysis of beach and dune sands. Sedimentology 60:1484–1497. https://doi.org/10.1111/sed.12040

Rose WI, Durant AJ (2009) Fine ash content of explosive eruptions. Journal of Volcanology and Geothermal Research 186:32–39. https://doi.org/10.1016/j.jvolgeores.2009.01.010

Rosin P, Rammler E (1933) The laws governing the fineness of powdered coal. Journal of the Institute of Fuel 7:29–36

Rossi E, Bonadonna C, Degruyter W (2019) A new strategy for the estimation of plume height from clast dispersal in various atmospheric and eruptive conditions. Earth and Planetary Science Letters 505:1–12. https://doi.org/10.1016/j.epsl.2018.10.007

Sanford RB, Swift DJP (1971) Comparison of Sieving and Settling Techniques for Size Analysis, Using a Benthos Rapid Sediment Analyzer. Sedimentology 17:257–264. https://doi.org/10.1111/j.1365-3091.1971.tb01778.x

Sarna-Wojcicki AM, Champion DE, Davis JO (1983) Holocene volcanism in the conterminous United States and the role of silicic volcanic ash layers in correlation of latest-Pleistocene and Holocene deposits. Late Quaternary environments of the United States 2:52–77

Sarna-Wojcicki AM, Shipley S, Waitt Jr RB, et al (1981) Areal distribution, thickness, mass, volume, and grain size of air-fall ash from the six major eruptions of 1980. US Geol Surv Prof Paper 1250:577–600

Sarocchi D, Sulpizio R, Macías JL, Saucedo R (2011) The 17 July 1999 block-and-ash flow (BAF) at Colima Volcano: New insights on volcanic granular flows from textural analysis. Journal of Volcanology and Geothermal Research 204:40–56. https://doi.org/10.1016/j.jvolgeores.2011.04.013

Saxby J, Beckett F, Cashman K, et al (2018) The impact of particle shape on fall velocity: Implications for volcanic ash dispersion modelling. Journal of Volcanology and Geothermal Research 362:32–48. https://doi.org/10.1016/j.jvolgeores.2018.08.006

Saxby J, Rust A, Beckett F, et al (2020) Estimating the 3D shape of volcanic ash to better understand sedimentation processes and improve atmospheric dispersion modelling. Earth and Planetary Science Letters 534:116075. https://doi.org/10.1016/j.epsl.2020.116075

Saxby J, Rust A, Cashman K, Beckett F (2019) The importance of grain size and shape in controlling the dispersion of the Vedde cryptotephra. Journal of Quaternary Science Special Issue: Intav Tephra: https://doi.org/10.1002/jqs.3152

Scarpati C, Sparice D, Perrotta A (2014) A crystal concentration method for calculating ignimbrite volume from distal ash-fall deposits and a reappraisal of the magnitude of the Campanian Ignimbrite. Journal of Volcanology and Geothermal Research 280:67–75. https://doi.org/10.1016/j.jvolgeores.2014.05.009

Schellenberg B, Richardson T, Watson M, et al (2019) Remote sensing and identification of volcanic plumes using fixed-wing UAVs over Volcán de Fuego, Guatemala. Journal of Field Robotics 36:1192–1211. https://doi.org/10.1002/rob.21896

Scollo S, Coltelli M, Prodi F, et al (2005) Terminal settling velocity measurements of volcanic ash during the 2002–2003 Etna eruption by an X-band microwave rain gauge disdrometer. Geophysical Research Letters 32:. https://doi.org/10.1029/2004GL022100

Sheridan MF (1971) Particle-size characteristics of Pyroclastic Tuffs. Journal of Geophysical Research (1896-1977) 76:5627–5634. https://doi.org/10.1029/JB076i023p05627

Sparks RSJ (1976) Grain size variations in ignimbrites and implications for the transport of pyroclastic flows. Sedimentology 23:147–188. https://doi.org/10.1111/j.1365-3091.1976.tb00045.x

Sparks RSJ, Brazier S, Huang TC, Muerdter D (1983) Sedimentology of the Minoan deep-sea tephra layer in the Aegean and Eastern Mediterranean. Marine Geology 54:131–167. https://doi.org/10.1016/0025-3227(83)90011-7

Sparks RSJ, Bursik MI, Ablay GJ, et al (1992) Sedimentation of tephra by volcanic plumes. Part 2: controls on thickness and grain-size variations of tephra fall deposits | SpringerLink. Bulletin of Volcanology 54:685–695. https://doi.org/10.1007/BF00430779

Sparks RSJ, Walker GPL (1977) The significance of vitric-enriched air-fall ashes associated with crystal-enriched ignimbrites. Journal of Volcanology and Geothermal Research 2:329–341. https://doi.org/10.1016/0377-0273(77)90019-1

Stevenson JA, Millington SC, Beckett FM, et al (2015) Big grains go far: understanding the discrepancy between tephrochronology and satellite infrared measurements of volcanic ash. Atmospheric Measurement Techniques 8:2069–2091. https://doi.org/10.5194/amt-8-2069-2015

Swineford A, Swineford F (1946) A comparison of three sieve shakers. Journal of Sedimentary Research 16:3–13. https://doi.org/10.1306/D426923D-2B26-11D7-8648000102C1865D

Visher GS (1969) Grain size distributions and depositional processes. Journal of Sedimentary Research 39:1074–1106

Vriend M, Prins MA (2005) Calibration of modelled mixing patterns in loess grain-size distributions: an example from the north-eastern margin of the Tibetan Plateau, China. Sedimentology 52:1361–1374. https://doi.org/10.1111/j.1365-3091.2005.00743.x

Walker GPL (1981) The Waimihia and Hatepe plinian deposits from the rhyolitic Taupo Volcanic Centre. New Zealand Journal of Geology and Geophysics 24:305–324. https://doi.org/10.1080/00288306.1981.10422722

Walker GPL (1980) The Taupo pumice: Product of the most powerful known (ultraplinian) eruption? Journal of Volcanology and Geothermal Research 8:69–94. https://doi.org/10.1016/0377-0273(80)90008-6

Walker GPL (1971) Grain-Size Characteristics of Pyroclastic Deposits. The Journal of Geology 79:696–714. https://doi.org/10.1086/627699

Watanabe K, Ono K, Sakaguchi K, et al (1999) Co-ignimbrite ash-fall deposits of the 1991 eruptions of Fugen-dake, Unzen Volcano, Japan. Journal of Volcanology and Geothermal Research 89:95–112. https://doi.org/10.1016/S0377-0273(98)00126-7

Webley PW, Stunder BJB, Dean KG (2009) Preliminary sensitivity study of eruption source parameters for operational volcanic ash cloud transport and dispersion models—A case study of the August 1992 eruption of the Crater Peak vent, Mount Spurr, Alaska. Journal of Volcanology and Geothermal Research 186:108–119

Weibull W (1951) A statistical distribution function of wide applicability. Journal of Applied Mechanics 293–297

Wen S, Rose WI (1994) Retrieval of sizes and total masses of particles in volcanic clouds using AVHRR bands 4 and 5. Journal of Geophysical Research: Atmospheres 99:5421–5431. https://doi.org/10.1029/93JD03340

Wentworth CK (1922) A scale of grade and class terms for clastic sediments. The journal of geology 30:377–392

Wiesner MG, Wetzel A, Catane SG, et al (2004) Grain size, areal thickness distribution and controls on sedimentation of the 1991 Mount Pinatubo tephra layer in the South China Sea. Bull Volcanol 66:226–242. https://doi.org/10.1007/s00445-003-0306-x

Williams SN, Self S (1983) The October 1902 plinian eruption of Santa Maria volcano, Guatemala. Journal of Volcanology and Geothermal Research 16:33–56. https://doi.org/10.1016/0377-0273(83)90083-5

Wilson TM, Stewart C, Sword-Daniels V, et al (2012) Volcanic ash impacts on critical infrastructure. Physics and Chemistry of the Earth, Parts A/B/C 45:5–23

WMO (2018) VAAC Operational Dispersion Model Configuration Snap Shot Version 3

Wohletz KH, Sheridan MF, Brown WK (1989) Particle size distributions and the sequential fragmentation/transport theory applied to volcanic ash. Journal of Geophysical Research: Solid Earth 94:15703–15721. https://doi.org/10.1029/JB094iB11p15703

Woods AW, Wohletz K (1991) Dimensions and dynamics of co-ignimbrite eruption columns. Nature 350:225

Yu Y (2018) mixR: Finite Mixture Modeling for Raw and Binned Data

Zdanowicz C, Zielinski G, Germani M (1999) Mount Mazama eruption: Calendrical age verified and atmospheric impact assessed. GEOLOGY 27:621–624. https://doi.org/10.1130/0091-7613(1999)027<0621:MMECAV>2.3.CO;2